DOI: 10.24850/j-tyca-2026-03-09

Articles

Application of techniques for detecting changes in land use and cover in the Pao River basin, Venezuela, using Landsat satellite images

Aplicación de técnicas de detección de cambios en el uso y la cobertura del suelo en la cuenca del río Pao, Venezuela, usando imágenes de satélites Landsat

Mairim Márquez-Romance[1], ORCID: https://orcid.org/0009-0000-9406-5611

Adriana Márquez-Romance[2], ORCID: https://orcid.org/0000-0003-1305-5759

Bettys Farías-de-Márquez[3], ORCID: https://orcid.org/0000-0002-7737-2545

Sergio Pérez-Pacheco[4], ORCID: https://orcid.org/0000-0001-6957-7287

Edilberto Guevara-Pérez[5], ORCID: https://orcid.org/0000-0003-2813-2147

[1]Centro de Investigaciones Hidrológicas y Ambientales, Universidad de Carabobo, Naguanagua, Carabobo, Venezuela, mmarquer@uc.edu.ve

[2]Centro de Investigaciones Hidrológicas y Ambientales, Universidad de Carabobo, Naguanagua, Carabobo, Venezuela, ammarquez@uc.edu.ve

[3]Centro de Investigaciones Hidrológicas y Ambientales, Universidad de Carabobo, Naguanagua, Carabobo, Venezuela, bfarias@uc.edu.ve

[4]Centro de Investigaciones Hidrológicas y Ambientales, Universidad de Carabobo, Naguanagua, Carabobo, Venezuela, sperez@uc.edu.ve

[5]Centro de Investigaciones Hidrológicas y Ambientales Universidad de Carabobo, Naguanagua, Carabobo, Venezuela, eguevara@uc.edu.ve

Corresponding author: Adriana Márquez-Romance, ammarquez@uc.edu.ve

Abstract

In this investigation, the spatio-temporal variation techniques were applied on the Pao river basin, located at the Venezuelan territory, through the satellite image processing. Eleven satellite images were acquired from Landsat satellite: L5TM, L7ETM SLC:on, and L8OLI. The change detection techniques were: post-classification and pre-classification applied on images from two dates: 1986-2016; 1990-2016; 1991-2016, 1998-2016, 1999-2016, 2000 SLC:on -2016, 2001-2016, 2002 SLC:on -2016, 2003 SLC:on-2016, 2015-2016. Seven pre-classification and a post-classification methods were applied. The categorization of the pre-classification methods in order of the more or less exact for estimating of the area proportion of change / no change in land cover and land uses from the Pao river basin obtained from the error matrix and by adjusting the methods to the local characteristics of the scene in the Landsat satellite image gave as a result: 1) principal component analysis 2) reflectance image differencing, 3) Kauth-Thomas transformation, 4) change vector, 5) reflectance image ratioing, 6) differencing of images of normalized difference of vegetation index and 7) reflectance image regression. In the post-classification method, the area difference corresponding to the Pao river basin between 1986 (date 1) and 2016 (date 2) gave the results about the classes following: Urban, -1.37 %; rangeland, -22.99 %; agricultural, 1.12 %; water, 0.55 %; vegetation, 8.1 %; degraded land, 9.66 %; clouds, 2.49 %; shadows, 2.28 %. The post-classification method has been the predominant option regarding to pre-classification method.

Keywords: land use, remote sensing, river basins, cartography, water resources, environmental degradation, Venezuela.

Resumen

En esta investigación se aplicaron técnicas de variación espacio-temporal de cobertura y uso en la cuenca del río Pao, localizada espacialmente en territorio venezolano, mediante procesamiento de imágenes satelitales. Se adquirieron 11 imágenes de satélite desde satélites Landsat: L5TM, L7ETM SLC (*Scan Line Corrector*, por sus siglas en inglés)-on, L8OLI. Las técnicas para detección de cambios han sido posclasificación y preclasificación aplicadas entre imágenes de dos fechas: 1986-2016; 1990-2016; 1991-2016, 1998-2016, 1999-2016, 2000 SLC:on-2016, 2001-2016, 2002 SLC:on-2016, 2003 SLC:on-2016, 2015-2016. Se aplicaron siete métodos de preclasificación y uno de posclasificación. La categorización de métodos de preclasificación en orden del más al menos exacto para estimación de proporción de área de cambio/ningún cambio bitemporal en coberturas y usos terrestres en la cuenca del río Pao obtenida a partir de matriz de error y ajuste de métodos a características locales de escena en imagen del satélite Landsat dieron como resultado:

1) análisis de componentes principales, 2) diferencia de imágenes de reflectancia, 3) transformación Kauth-Thomas, 4) vector de cambio, 5) relación de imágenes de reflectancia, 6) diferencia de imágenes de índice de vegetación de diferencia normalizada y 7) regresión de imágenes de reflectancia. En el método de posclasificación, la diferencia de área correspondiente a la cuenca del río Pao entre 1986 (fecha 1) y 2016 (fecha 2) dio los siguientes resultados en clases: urbano, -1.37 %; agropecuario, -22.99 %; agrícola, 1.12 %; agua, 0.55 %; vegetación, 8.1 %; suelo degradado, 9.66 %; nubes, 2.49 %; sombras, 2.28 %. El método posclasificación ha sido la opción predominante con respecto a métodos de preclasificación.

Palabras clave: uso de la tierra, teledetección, cuencas hidrográficas, cartografía, recursos hídricos, degradación ambiental, Venezuela.

Received: 11/11/2024

Accepted: 08/08/2025

Available ahead of print: 04/09/2025

Version of record: 01/05/2026

Introduction

Information on spatiotemporal variation in land cover and land use is important because of its practical uses in applications such as monitoring the removal or permanent reduction of forest stand, usually for other land uses such as agriculture, livestock, urbanization or mining, disaster monitoring, urban expansion, land planning and management (Hussain, Chen, Cheng, Wei, & Stanley, 2013). Singh (1989) defined change detection as "the process of identifying differences in the state of an object or phenomenon by observing it at different times." Land cover and use change detection techniques can be grouped as: pre-classification and post-classification (Chen, Chen, Shi, & Yamaguchi, 2012).

The characterization of land use and land cover allows for the selection of the boundaries of the area to be mapped depending on the study objective. Watersheds are a suitable spatial framework for the study of ecosystems; they are a water-producing unit for natural and anthropogenic uses (Guevara & Cartaya, 2004). Whether independently or interconnected with others, watersheds are excellent units for the integrated management of goods and services provided by ecosystems that are altered when land use/cover changes.

In recent years, satellite-based sensing has become a suitable tool for describing land use/cover characteristics over large areas (Townshend, Justice, Li, Gurney, & McManus, 1991). The images generated by these sensors provide qualitative and spatially continuous data of the surface, making them particularly useful for describing land use over large areas. The discrimination of land cover types (summer crops, winter crops, forested woodland, water bodies, pastures, etc.) is based on the uniqueness of their spectral response and the temporal changes that may occur within them (Guerschman, Paruelo, & Burke, 2003).

The objective of this study was to describe the spatial and temporal variation of land use and land cover transformations in the Pao River basin, using information from airborne devices (satellites) from Landsat *L5TM/L7ETM /L8OLI sensors;* between the periods 1986-2016; 1990-2016; 2000-2016, applying post-classification and pre-classification change detection techniques.

The importance of applying various change detection techniques to remote sensing products lies in the recognition/identification of an object or several characteristics in its surroundings (Joseph, 2005). The characteristic that allows the recognition/identification of an object and its surroundings is achieved from the differences between the reflectance/radiance/emittance characteristics with respect to a wavelength (spectral signature). Temporal changes in the spectral signature can act as a characteristic signal in the discrimination of certain types of objects monitored by remote sensing (Joseph, 2005).

The basic premise of using remote sensing data for land cover change detection is that changes in reflectance/radiance values are detected, and the changes in reflectance/radiance due to land cover change must be large due to changes in reflectance/radiance caused by other factors. These other factors include (1) differences in atmospheric conditions, (2) differences in sun angle, and (3) differences in soil moisture (Singh, 1989).

Various land cover change detection methods using digital satellite data have been proposed, which could assist in updating resource inventories. The diversity of methods has depended on the requirements and conditions. However, selecting the most appropriate method or algorithm for change detection is not easy in practice (Hussain *et al*., 2013). The methods can involve pixel-based (Mas, 1999) and object-based (Araya & Hergaten, 2008) methods. Pixel-based methods include direct comparison, image transformation, change detection-based classification, geographic information systems, and enhanced object-based methods. Object-based methods include those based on object comparison and direct object classification comparison. In this study, the main pixel-based methods were applied, covering land cover classification comparison, multitemporal classification, image relation/difference, vegetation index differentiation, principal component analysis, and change vector analysis.

Materials and methods

Study region

The Pao River basin is contained in the states of Cojedes, Carabobo and Aragua, Venezuelan territory, whose water network flows into the Orinoco River, it has a total area of 3 018.54 km^2 (De-Márquez-Farías & Márquez-Romance, 2023). The basin includes fourteen main rivers and three reservoirs (Figure 1), which provide water for the development of land uses in the three states, whose urban population is as follows (De-Márquez-Farías & Márquez-Romance, 2023): 1) Cojedes, 265,541 inhabitants, 2) Carabobo, 2,208,188 inhabitants and 3) Aragua, 1,557,151 inhabitants. Land cover/land use according to the US Geological Survey (USGS) Land Classification System for use with remote sensing data are five main ones: 1) urban, 2) agricultural, 3) livestock, 4) forest and 5) water (Anderson, Hardy, Roach, & Witmer, 1976).

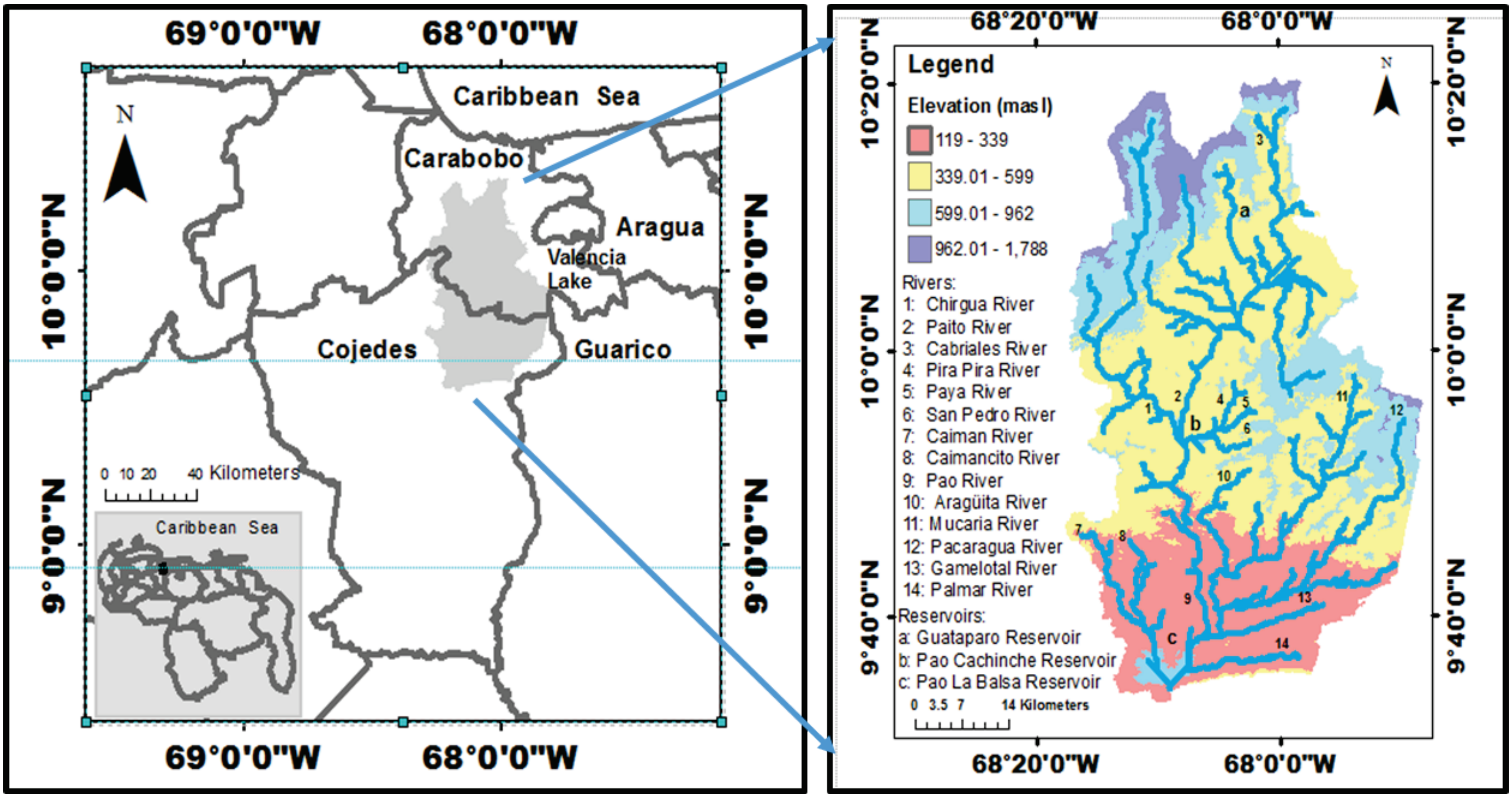

Figure 1. Spatial location of the Pao River basin in the states of Cojedes, Carabobo, and Aragua, Bolivarian Republic of Venezuela. Source: De-Márquez-Farías and Márquez-Romance (2023).

This section describes the following stages (De-Márquez-Farías & Márquez-Romance, 2023). **In the first stage**, the procedures for acquiring satellite images and their characteristics are described; as well as the reference images of land uses and covers in the Pao River basin; justifying the assigned classes. **In the second stage**, the preliminary processing of satellite images using absolute and relative corrections is described. **In the third stage**, the application of change detection techniques: 1) Post-classification, 2) Pre-classification and the Preliminary data processing in the context of the study. **In the fourth stage**, a threshold analysis is performed, based on fitting the data to a normal probability distribution function. The change/no change thresholds are used in the pre-classification methods. **In the fifth stage**, the results of the change detection methods are compared (De-Márquez-Farías & Márquez-Romance, 2023).

Satellite information data acquisition and validation

Eleven images of a single scene from the Landsat satellite array associated with the dry season months between November and April of each year were acquired from the EarthExplorer digital portal (De-Márquez-Farías & Márquez-Romance, 2023). The scene contains the entire Pao River basin. The set of images acquired over time by the Landsat satellite group has been selected as described below (Table 1): 1) L5-Thematic Mapper (1986, 1990, 1991, 1998, 2001), 2) L7-Enhanced Thematic Mapper-SLC:on (1999, 2000, 2002, 2003) and 3) L8 -Opertional Land Imager (2015 and 2016) (De-Márquez-Farías & Márquez-Romance, 2023).

Table 1. Characteristics of the Landsat satellite images used in this research.

No.	Scene Code	Acquisition Date	Time the scene center was taken	Cloud Cover	Image Quality	Solar Azimuth	Solar Zenith
1	LT50050531986351XXX03	1986-12-17	14:11:28.3900750Z	20.00	7	134.93319530	42.24871979
2	LT50050531990010CPE03	1990-01-10	14:15:12.2020810Z	11:00	7	131.96692328	41.77289720
3	LT50050531991077CPE01	1991-03-18	14:14:04.6490630Z	28.00	7	104.58761331	51.37583561
4	LT50050531998032CPE00	1998-02-01	14:28:28.6110190Z	33.00	9	127.94531961	46.11991603
5	LT50050531999019CPE00	1999-01-19	14:31:37.3780560Z	23.00	9	132.94664692	45.23014868
6	LE70050532000014SGS01	2000-01-14	14:45:26.0198689Z	7.00	9	137.52485114	47.22916723
7	LT50050532001008AAA02	2001-01-08	14:32:22.5760750Z	10.00	9	135.84219087	44.77755780
8	LE70050532002051AGS00	2002-02-20	14:41:26.1414958Z	22.00	9	122.73905080	52.13911206
9	LE70050532003022PFS00	2003-01-22	14:41:05.9709036Z	10.00	9	134.07217263	47.15930857
10	LO80050532015063LGN00	2015-03-04	14:52:20.8148112Z	13.13	9	119.09567247	57.19634293
11	LC80050532016018LGN00	2016-01-18	14:52:41.9360648Z"	6.09	9	138.18721946	48.77317194

Source: De-Márquez-Farías and Márquez-Romance (2023).

According to Chander, Markham and Helder (2009), all ETM+ acquisitions after 31 May 2003 exhibit an anomaly caused by the failure of the Scan Line Corrector (SLC), which compensated for the spacecraft's forward motion so that all scans were aligned in parallel. Images with data loss are called SLC-off images, while images acquired before the SLC failure are called SLC-on images (i.e., without data gaps). The malfunction of the SLC mirror array resulted in the loss of approximately 22 % of the scene normal area.

The image of the Pao River basin is identified under the World Reference System according to the route and row as follows: 005 and 053, respectively. The map projection parameters according to the United

States Geological Survey are: 1) Projection: UTM, 2) Datum: WGS1984, 3) Ellipsoid: WGS84, 4) UTM Zone: 19 N, 5) Cubic convolution. The characteristics of the images acquired according to each satellite are identified in Table 2. The reference data consist of Google Earth images. The characteristics of the acquired images and photographs based on: date, coordinates, use and land cover are shown in Figure 2 (De-Márquez-Farías & Márquez-Romance, 2023).

Table 2. Composition of the spectral bands of the Landsat satellite image for the Pao River basin scene

Landsat 5 TM			**Landsat 7 ETM**			**Landsat 8 OLI**		
Spectral band	**Spectral range**	**Grid cell size**	**Spectral band**	**Spectral range**	**Grid cell size**	**Spectral band**	**Spectral range**	**Grid cell size**
Unit	**µm**	**m**	**Unit**	**µm**	**m**	**Unit**	**µm**	**m**
B1	0.452-0.518	30	B1	0.452-0.514	30	B1	0.43 – 0.45	30
B2	0.528-0.609	30	B2	0.519-0.601	30	B2	0.45 – 0.51	30
B3	0.626-0.693	30	B3	0.631-0.692	30	B3	0.53 – 0.59	30
B4	0.776-0.904	30	B4	0.772-0.898	30	B4	0.64 – 0.67	30
B5	1.567-1.784	30	B5	1.547-1.748	30	B5	0.85 – 0.88	30
B6	10:45-12:42	30	B6	10:31-12:36	30	B6	1.57 – 1.65	30
B7	2.097-2.349	30	B7	2.065-2.346	30	B7	2.11 – 2.29	30

Source: De-Márquez-Farías and Márquez-Romance (2023).

a) 25/01/2017. Agua 10°10’45.81”N, 68°03’54”O b) 20/04/2017. Urbano 10°14’17.89”N, 68°0’35.26”O

c) 17/02/2017. Agropecuario 10°02’16.99” N, 68°24.26”O d) 30/12/1989. Agrícola 10°13’47.08”N, 68°11’28.18”O

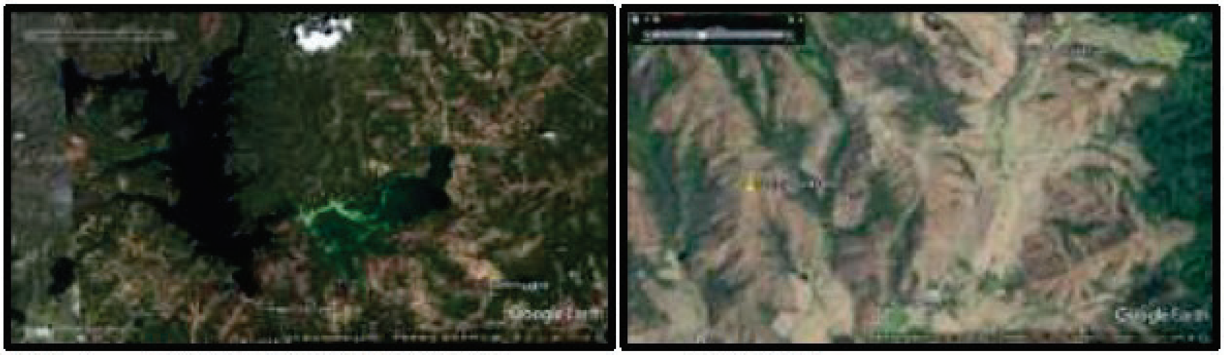

e) 30/12/1987 .Agua 9°53’49.06”N, 68°06’55.77”O f) 30/12/1989. Suelo Degradado 10°16’0.01”N, 68°12’7.29”O

Figure 2. Sample of reference images extracted from Google Earth corresponding to the land covers/uses classified in the Pao River basin. Source: De-Márquez-Farías and Márquez-Romance (2023).

Preliminary image processing

Preliminary processing of Landsat satellite images involves performing absolute and relative corrections on each image, as follows: geometric, radiometric, topographic, and atmospheric. Applying the correction algorithms to the set of spectral bands that make up the image in a sequential batch execution requires compositing the spectral bands in each Landsat satellite image using the ArcGIS v.10.0 computational tool. The spectral radiometric bands included in the composition for each Landsat satellite are as indicated in Table 2 (De-Márquez-Farías & Márquez-Romance, 2023).

Absolute and relative image corrections

In this research, the images have been obtained in a geometrically corrected version from the USGS. The radiometric, topographic, and absolute atmospheric corrections applied to each image are executed in the ENVI 4.7 satellite image processing computational tool environment. The relative corrections between images from the different sensors of the Landsat satellite set mainly include geometric and radiometric corrections, for example, the relative geometric corrections are based on a procedure known as image-to-image registration (De-Márquez-Farías & Márquez-Romance, 2023).

The ATCOR module (Atmospheric and Topographic Corrections) (Richter & Schläpfer, 2019) was used to apply radiometric, atmospheric, and topographic corrections. Figure 3 shows the main processing steps required to compensate for atmospheric and topographic effects. The input data consists of the recorded scene plus a meta-file containing the acquisition date, time, solar and sensor view geometry, among others. Input data are typically in TIF or JP2 format, in a single file or in separate files for each band. In most cases, they represent a scaled radiance, called a Digital Number (DN), where the radiance L can be obtained with the radiometric shift c_0 and the gain c_1:

$$L = c_0 + c_1 DN \tag{1}$$

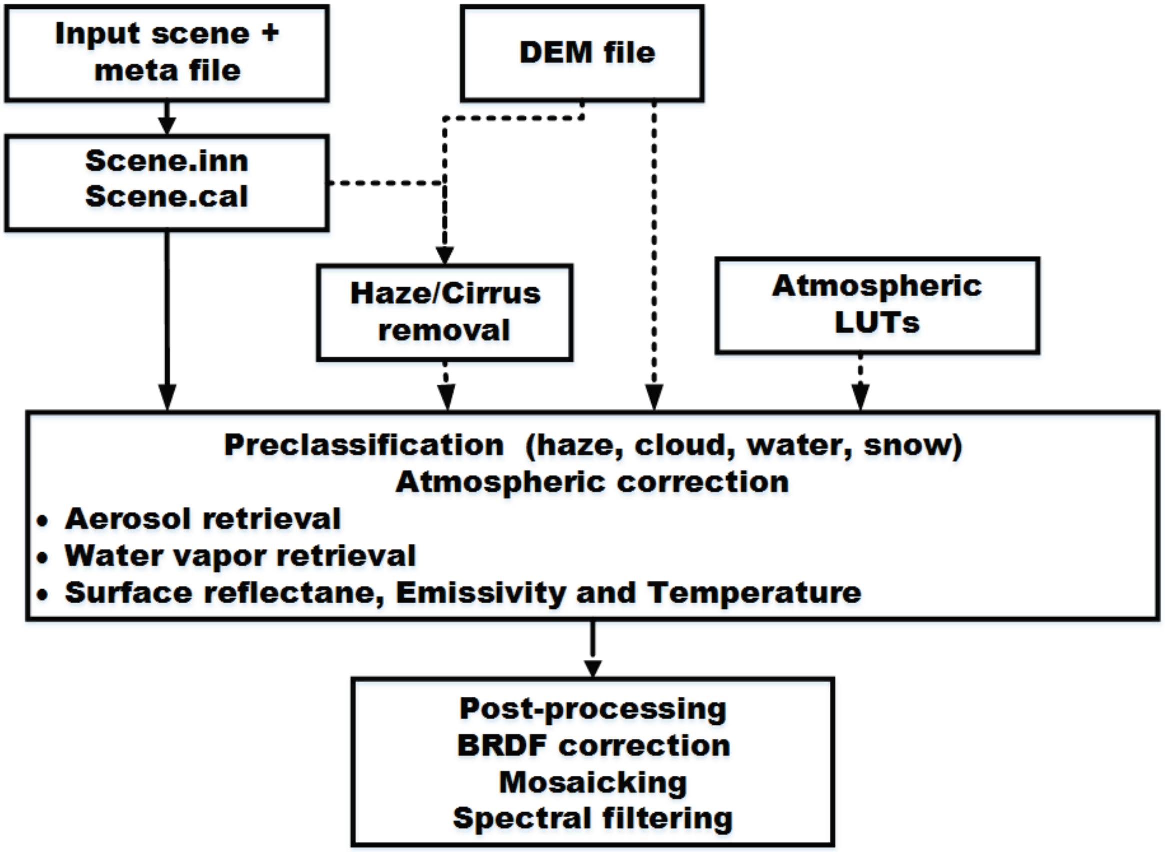

Figure 3. Main steps of atmospheric corrections. Source: Adapted from Richter and Schläpfer (2019).

For some instruments, data is delivered as top-of-atmosphere reflectance (TOA). ρ_{TOA}:

$$\rho_{TOA} = \frac{\pi L d^2}{E_s \cos\theta_s} \qquad (2)$$

Where:

d = Earth-Sun distance (astronomical units)

E_s = extraterrestrial solar irradiance

θ_s = solar zenith angle

ATCOR converts TOA reflectance to TOA radiance before starting the atmospheric correction.

The main steps of atmospheric correction processing are shown in Figure 3. The input image scene is converted to ENVI band sequential format, the necessary parameters are extracted from the image metafile and stored in the scene.inn file, and the radiometric calibration (c_0, c_1) per band is stored in scene.cal.

For a mountain scene, the DEM (Digital Elevation Model) must be provided. Dashed lines indicate optional processing steps, e.g., haze/cirrus removal. For standard sensors (e.g., Landsat, Sentinel-2, Worldview, etc.), atmospheric lookup tables are already available. The main block consists of pre-classification, followed by atmospheric/topographic correction. In some cases, post-processing is required.

Change detection methods

The change detection methods applied in this research are (De-Márquez-Farías & Márquez-Romance, 2023): 1) **Post-classification method,** based on the thematic classification of two different images of dates independently. The thematic maps are subsequently compared and analyzed to correlate the type of change (Lunetta, Lyon, Guindon, & Elvidge, 1998; Yuan, Sawaya, Loeffelholz, & Bauer, 2005). 2) **Pre-classification methods**, the following were selected: a) **Algebraic**: image difference, image relation, image regression, image difference of vegetation index and change vector and b) **Transformation**: difference of principal components analysis, difference of images from the Kauth-Thomas transformation method and its modifications (De-Márquez-Farías & Márquez-Romance, 2023).

Image differentiation

Two precisely coregistered multitemporal images are used to generate a residual image representing the changes. The difference can be measured directly from the pixel's radiometric values or in extracted, derived, or transformed images, such as texture or vegetation indices (Hussain *et al*., 2013). Mathematically, the difference image is:

$$Dx_{ij}^{k} = x_{ij}^{k}(t_2) - x_{ij}^{k}(t_1) + C \qquad (3)$$

Where:

x_{ij}^{k} = pixel value for spectral band

k, i, j = line and pixel numbers in the image

t_1 = first date

t_2 = second date

C = constant to produce positive digital numbers

Pixels that show radiance changes are located at the tails of the distribution, while pixels that do not show radiance changes tend to cluster around the mean (Singh 1989).

Relationship of images

Calculates the relationship between two images recorded at different times with one or more bands, band by band. The data is compared pixel by pixel (Singh, 1989). Mathematically:

$$Rx_{ij}^{k} = \frac{x_{ij}^{k}(t_1)}{x_{ij}^{k}(t_2)} \tag{4}$$

Where $x_{ij}^{k}(t_2)$ is the pixel value of band k for pixel x in row i and column j at time t = $_2$. If the intensity of the reflected energy is virtually the same in each image, then $Rx_{ij}^{k} = 1$, this indicates no change. In areas with changes, the ratio value would be significantly greater or less than 1, depending on the nature of the changes between the two dates (Nelson, 1983).

Image regression

The pixels of time (t_1) are a linear function of pixels in time (t_2). It can be regressed $x_{ij}^{k}\ (t_1)$ against $x_{ij}^{k}\ (t_2)$ using least squares regression (x is the pixel value of line i, column j of band k). If $x_{ij}^{k}\ (t_2)$ is the predicted value obtained from the regression line, the difference image can be defined as follows (Singh 1989):

$$\hat{x}_{ij}^{k}(t_2) = a x_{ij}^{k}(t_1) + b \tag{5}$$

$$D x_{ij}^{k} = \hat{x}_{ij}^{k}(t_2) - x_{ij}^{k}(t_1) \tag{6}$$

Vegetation index differentiation

Vegetation indices are mathematical transformations designed to assess the impact of vegetation on multispectral observations. These indices enhance spectral differences based on vegetation's high absorbance in the red and high reflectance in the near-infrared (Hussain *et al*., 2013). For change detection, vegetation indices are typically generated separately for two images, and then standard pixel-based change detection (e.g., differencing or ratio) is applied. Different vegetation indices have been developed, such as the Normalized Difference Vegetation Index (NDVI) by Rouse, Haas, Schell and Deering (1974), as follows:

$$NDVI = \frac{\rho_{nir} - \rho_{red}}{\rho_{nir} + \rho_{red}} \tag{7}$$

Where:

ρ_{red} = radiant flux reflected in red

ρ_{nir} = radiant flux in near infrared

Change vector analysis

The vector describing the direction and magnitude of the change between the first and second dates is a spectral shift vector. A change is considered to have occurred if the magnitude of the calculated spectral shift vector exceeds a specified threshold (Malila, 1980).

Principal component analysis

Principal component analysis (PCA), mathematically based on the Principal Axis Transformation, is a transformation of multivariate data into a new set of components, thereby reducing data redundancy (Lillesand, Kiefer, & Chipman, 2014). PCA uses either a covariance matrix or a correlation matrix to transform data into an uncorrelated set. The eigenvectors of the resulting matrices are sorted in decreasing order, with the first principal component (PC) expressing most of the variation in the data (Hussain *et al*., 2013). In PCA, areas with no change are assumed to be highly correlated, while areas with changes are uncorrelated. In multitemporal image analysis, PC1 and PC2 tend to represent areas with no change, while PC3 and subsequent PCs contain the change information (Byrne, Crapper, & Mayo, 1980; Ingebritsen & Lyon, 1985). The CPs of the images are obtained separately and then another change detection technique, such as image differencing, is used.

Kauth-Thomas transformation

Kauth and Thomas (1976) produced an orthogonal transformation of the original Landsat MSS data space to a new four-dimensional feature space. This transformation was termed the Kauth-Thomas or Tasseled Cap transformation. Crist and Kauth (1986) obtained visible, near-infrared, and mid-infrared coefficients for transforming Landsat Thematic Mapper imagery into brightness, greenness, and wetness variables. Huang, Wylie, Yang, Homer and Zylstra (2002) developed Tasseled Cap coefficients for use with Landsat 7 Enhanced Thematic Mapper Plus on satellite reflectance data. Change is measured based on brightness, greenness, and wetness values (Lu, Mausel, Brondízio, & Moran, 2004):

$$B = 0.2909\,TM1 + 0.2493\,TM2 + 0.4806\,TM3 + 0.5568\,TM4 + 0.4438\,TM5 + 0.1706\,TM7 \qquad (8)$$

$$G = -0.2728\,TM1 - 0.2174\,TM2 - 0.5508\,TM3 + 0.7221\,TM4 + 0.0733\,TM5 - 0.1648\,TM7 \qquad (9)$$

$$W = 0.1446\,TM1 + 0.1761\,TM2 + 0.3322\,TM3 + 0.3396\,TM4 - 0.6210\,TM5 - 0.4186\,TM7 \qquad (10)$$

Post-classification comparison

It compares two classified images to generate a change matrix. It is often used as a benchmark for the qualitative evaluation of emerging CD techniques (Lunetta *et al*., 1998). The classified images are subsequently compared to measure changes (Hussain *et al*., 2013). The classes of both images must be identical to llow a direct comparison. Classification errors from each image propagate into the final change map, reducing the accuracy of the final CD (Chan, Chan, & Yeh, 2001; Lillesand *et al*., 2014).

Determining thresholds for change detection

A commonly used method involves selecting appropriate threshold values using the standard deviation from the mean and testing the results empirically (Sinha & Kumar, 2013). In this research, thresholding was performed in three steps using ArcGIS V. 10.0 (De-Márquez-Farías & Márquez-Romance, 2023): 1) Once the change detection technique was applied, the resulting image was reclassified into three classes, including the mean class and classes where the values exceed one time the standard deviation. 2) The Change/No Change map is obtained using a threshold assumed to be one time the standard deviation. 3) The statistics of the Change/No Change zones are estimated using the Zonal Statistics as Table tool. The number of pixels and the linked area where Change/No Change has been observed are estimated.

Comparison of results with conventional techniques

The comparison of results is carried out between the two proposed methods: post-classification and pre-classification of bitemporal satellite images in order to select the one that allows quantifying the changes in land cover classes and uses in the Pao River basin (De-Márquez-Farías & Márquez-Romance, 2023).

Results

Results of the post-classification method

The results of the post-classification comparison are shown in Figure 4; from Figure 4a to Figure 4j it is shown that the classified images permanently reflect the following uses (De-Márquez-Farías & Márquez-Romance, 2023): a) urban, b) agricultural, c) agricultural, d) water, e) degraded soil, f) vegetation, g) clouds, h) shade and i) unclassified. The evaluation of the accuracy in the classification of each reflectance image is as shown in Table 3. The sample consists of 512 pixels randomly selected from the 2016 Landsat 8OLI image. The sample size of the pixels was determined by a mesh of random points separated every 1000 meters using the *Create Random Points tool contained in the Arctoolbox →Data Management Tools →Feature Class →menu. Create Random Points* from ArcGIS V.-10.0 software. The unclassified pixels were 164. The pixels in the classified map, user accuracy and Kappa index are: a) urban: 18, 88.90 %, 0.88; b) agricultural: 100, 99.00 %, 0.98; c) agricultural: 1, 100.00 %, 1; d) water: 4, 100.00 %, 1; e) vegetation: 165, 100.00 %, 1; f) degraded soil: 57, 98.25 %, 0.98; g) clouds: 2, 100.00 %, 1; h) shadows: 1, 100.00 %, 1 (De-Márquez-Farías & Márquez-Romance, 2023).

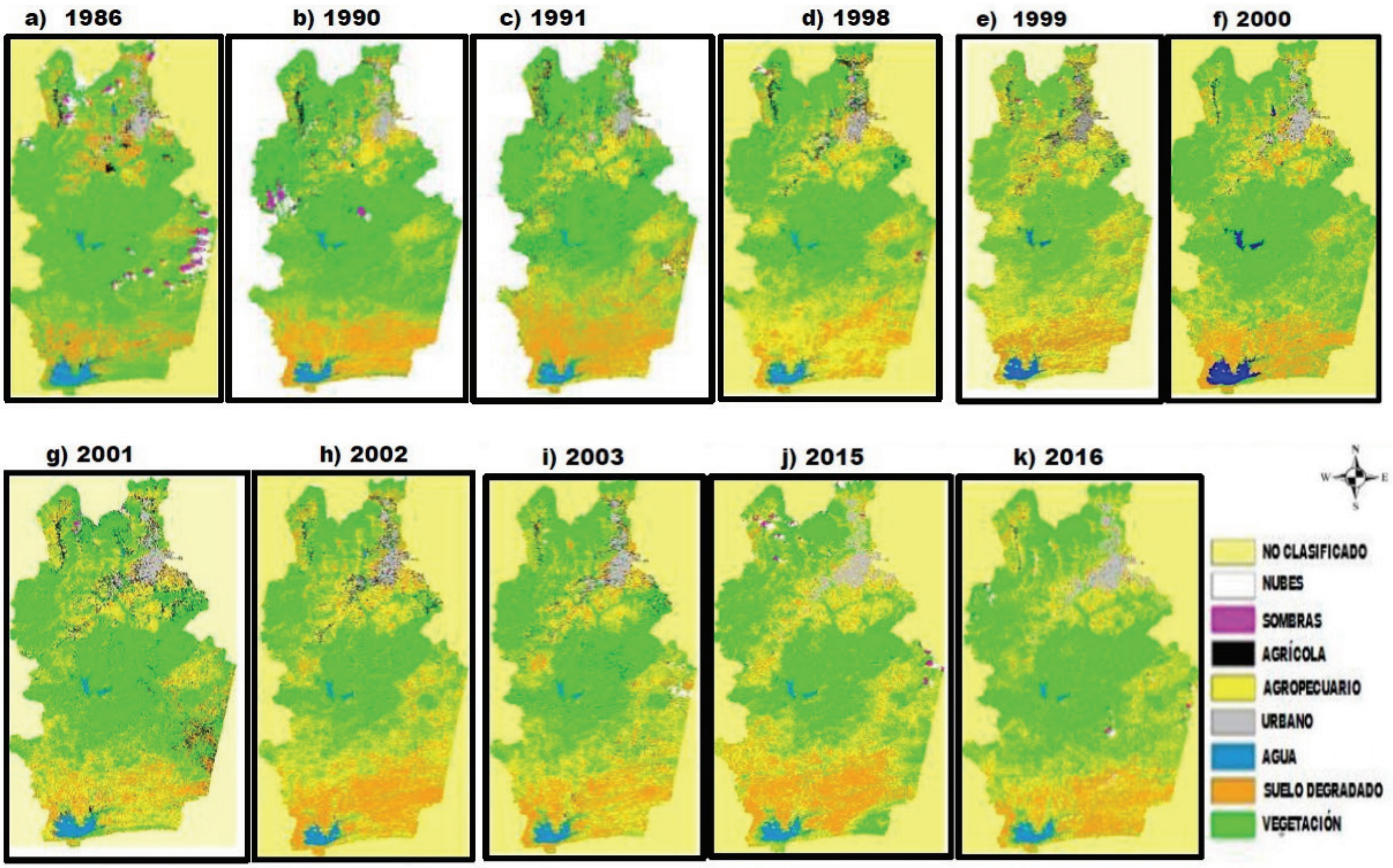

Figure 4. Results of the post-classification comparison method expressed through land use and land cover maps of the Pao River basin applied to Landsat satellite reflectance images, period 1986-2016: a) 1986, b) 1990, c) 1991, d) 1998, e) 1999, f) 2000, g) 2001, h) 2002, i) 2003, j) 2015 and k) 2016. Source: De-Márquez-Farías and Márquez-Romance (2023).

Table 3. Results of the post-classification comparison method expressed through the error matrix corresponding to the land use and land cover classification maps obtained based on reflectance images in the Pao River basin from 1986 to 2016. The results of the error matrix include the comparison of 512 randomly selected pixels on the classified map –left column- with respect to the uses observed in the Google Earth 2016 reference image –top row-. The classes are: 1. Unclassified; 2. Urban; 3. Agricultural; 4. Agricultural; 5. Water; 6. Vegetation; 7. Degraded soil; 8. Clouds; 9. Shadows.

	Land Use	**Reference Data**											
		2016											
		1	**2**	**3**	**4**	**5**	**6**	**7**	**8**	**9**	**Total in Rows**	**User Accuracy (%)**	**Kappa Total**
Classified Map	**1**	164									164		1
	2		16	1				1			18	88.89	0.8853
	3			99			1				100	99	0.9875
	4				1						1	100	1
	5					4					4	100	1
	6						165				165	100	1
	7			1				56			57	98.25	0.9803
	8								2		2	100	1
	9									1	1	100	1
Total in Column		164	16	101	1	4	165	57	2	1	**512**		
Producer Accuracy (%)			100	98.02	100	100	99.4	98.25	100	100		99.22	
Total Kappa Index													0.9895

Source: De-Márquez-Farías & Márquez-Romance (2023).

The pixels in the reference image and the producer accuracy are (De-Márquez-Farías & Márquez-Romance, 2023): a) urban: 16, 100 %;

b) agricultural: 101, 98.02 %; c) agricultural: 1, 100 %; d) water: 4, 100 %, 1; e) vegetation: 165, 99.4 %; f) degraded soil: 57, 98.25 %; g) clouds: 2, 100 %, 1; h) shadows: 1, 100 %. The overall accuracy index is 99.22 % and the Total Kappa index is 0.98.

The accuracy evaluation indexes of the eleven classified images corresponding to overall accuracy and Kappa index are as follows: 1) 1986: 98.04 %, 0.97; 2) 1990: 99.20 %, 0.99; 3) 1991: 98.83 %, 0.98; 4) 1998: 99.02 %, 0.98; 5) 1999: 98.83 %, 0.98; 6) 2000: 99.22 %, 0.99; 7) 2001: 93.00 %, 0.96; 8) 2002: 99.22 %, 0.99; 9) 2003: 99.3 %, 0.99; 10) 2015: 99.4 %, 0.99; 10) 2016: 99.22 %, 0.99.

The bitemporal difference in occupied areas according to the class expressed as a percentage corresponding to the Pao River basin from 1986 to 2016 is shown in Table 4; where the following results are observed in the classes urban (1), agricultural (2), agricultural (3), water (4), vegetation (5), degraded soil (6), clouds (7), shadows (8).

Table 4. Results of the post-classification comparison method expressed as the difference in bitemporal percentage proportion of land cover areas and land uses in the Pao River basin from 1986 to 2016.

Bitemporal images	Urban (1)	Rural (2)	Agricultural (3)	Water (4)	Vegetation (5)	Deforested land (6)	Cloud (7)	Shadow (8)
1986-2016	-1.37	-22.99	1.12	0.55	8.10	9.66	2.49	2.28
1990-2016	-1.76	-14.33	2.69	0.14	4.99	5.75	0.47	1.90
1991-2016	-1.25	-11.71	4.97	0.20	-3.70	11.56	-0.16	-0.07
1998-2016	-1.04	-2.45	0.93	0.23	-6.96	9.81	-0.55	0.04
1999-2016	-1.76	-14.33	2.69	0.14	4.99	5.75	0.47	1.90
2000-2016	-1.83	-10.57	1.26	0.54	2.25	9.48	-0.84	-0.27
2001-2016	-0.90	-5.13	4.46	0.20	0.12	0.60	-0.44	0.41
2002-2016	-0.86	-4.93	4.46	0.21	0.43	0.73	-0.44	0.41
2003-2016	-1.28	-0.27	2.78	0.10	-3.67	2.84	-0.23	-0.28
2015-2016	-0.49	3.02	-0.32	-0.15	4.17	-5.69	-0.06	-0.45

Source: De-Márquez-Farías & Márquez-Romance (2023).

The results of the proportion of areas in the maps obtained from the post-classification method in the Pao River basin in terms of Change/No Change are as follows, as a sample (Table 5): *1986-2016:* Change: Count: 1563761; RPA: 32.60 %. No Change: Change: Count: 3233594; RPA: 67 (De-Márquez-Farías & Márquez-Romance, 2023).

Table 5. Results of the post-classification method expressed by the change matrix corresponding to the proportion of Change/No Change areas in the maps obtained from the processed reflectance images of the Pao River basin, period 1986-2016.

	1986-2016		**1990-2016**		**1991-2016**		**1998-2016**		**1999-2016**	
	Change	**No change**	**Change**	**No change**	**Change**	**No change**	**Change**	**No change**	**Change**	**No change**
Count	1563761	3233594	1312310	3482890	1437425	1777485	1309996	1904915	1235080	1979282
Percentage area ratio (PAR) (%)	32.60	67.40	27.37	72.63	44.71	55.29	40.75	59.25	38.42	61.58

Table 5 (continued). Results of the post-classification method expressed by the change matrix corresponding to the proportion of Change/No Change areas in the maps obtained from the processed reflectance images of the Pao River basin, period 1986-2016.

	2000-2016		**2001-2016**		**2002-2016**		**2003-2016**		**2015-2016**	
	Change	**No change**	**Change**	**No change**	**Change**	**No change**	**Change**	**No change**	**Change**	**No change**
Count	1183899	2031012	1334471	1880445	1211899	2003012	1183899	2031012	2838542	1955557
Percentage area ratio (PAR) (%)	36.83	63.17	41.51	58.49	37.70	62.30	36.83	63.17	59.2091	40.790918

Results of pre-classification methods: algebraic for change detection

Results of the reflectance image difference method

As a sample, this section includes the results of the difference method for bitemporal reflectance images expressed as interval boundaries for the distribution of pixels in the areas of change/no change in the Pao River basin from 1986 to 2016 (Table 6). The criterion for setting these boundaries for the areas of change/no change is as follows: In the first: mean (μ) +/- 1 standard deviation (σ). In the second: < μ-1σ, > μ+1σ; respectively. The intervals represented by: mean, standard deviation, change intervals **<μ – 1σ,** no-change interval: μ +/ – 1σ, change intervals **>μ + 1σ** found for the difference of bitemporal reflectance images are, as a sample: *1986-2016:* 1.71, 6.58, -85- -8, -8-12, 12-89. In Table 6 it can be observed that the difference of the bitemporal images tends to be symmetrical with mean approximately zero as in the periods: 1986-2016, 1990-2016, 1991-2016, 1998-2016, 1999-2016, 2001-2016 and 2015-2016; finding bias or asymmetry in the following periods: 2000-2016, 2002-2016, 2003-2016 (De-Márquez-Farías & Márquez-Romance, 2023).

Table 6. Results of the difference method of bitemporal reflectance images expressed by interval limits for the distribution of pixels of Change/No Change areas in the Pao River basin from 1986 to 2016.

Bitemporal Images	**1986-2016**	**1990-2016**	**1991-2016**	**1998-2016**	**1999-2016**	**2000-2016**	**2001-2016**	**2002-2016**	**2003-2016**	**2015-2016**
μ	1.71	0.06	-0.37	-1.1	-0.13	-5.2	0.19	-6.1	-6.8	1.93
σ	6.58	4.86	5.05	4.66	4.65	5.43	4.91	6.1	6.36	4.98
LI: $< \mu - 1\sigma$	-85- -8	-90- -7	-79- -8	-84- -8	-79- -7	-85- -13	-78- -7	-83- -14	-87—16	-87- -6
NC: μ +/- 1σ	-8-12	-7-7	-8-7	-8-6	-7-7	-13-3	-7-8	-14-2	-16-3	-6-9
LS: $> \mu + 1\sigma$	12-89	7-87	7-77	6-87	7-85	3-53	8-80	2-73	3-83	9-87

Source: De-Márquez-Farías and Márquez-Romance (2023).

The results of the bitemporal reflectance image difference method expressed by the error matrix in the classification accuracy in the Pao River basin from 1986 to 2016 are shown in Table 7; where the following correspondence is observed between the pixels in the classified map (MC) of land covers (CT) and land uses (UT) under the following three categories: Decrease (DIS), No Change (NC) and Increase (INC) and the reference data (DR) based on the corrected images of Landsat 5TM, Landsat 8OLI and Google Earth associated with these three categories for a sample of 411 points, as a sample: 1) DIS in MC corresponding to DIS in DR: 86, DIS in MC corresponding to NC in DR: 82, DIS in MC corresponding to INC in DR: 0. The overall accuracy and Kappa indices are: 70.56 % and 0.6112, respectively (De-Márquez-Farías & Márquez-Romance, 2023).

The result of the application of the reflectance image difference method in the Pao River basin bitemporal 1986-2016 is shown in Figure 5 (De-Márquez-Farías & Márquez-Romance, 2023).

Table 7. Results of the bitemporal reflectance image difference method expressed by the error matrix on classification accuracy in the Pao River basin from 1986 to 2016.

Classified data		**Reference data (RD)**			**Total classifieds**	**User accuracy (%)**	**K**
		DIS	**NC**	**INC**			
Difference in Reflectance Images 1986-2016							
MC CT/UT	**DIS**	86	82	0	168	51.19	0.047
	NC	0	57	0	57	100.00	1,000
	INC	0	39	147	186	79.03	0.790
	Totals in the reference	86	178	147	411		
	Producer accuracy (%)	100	32.02	100			
Global classification accuracy (%)							70.56
Global Kappa statistics							0.612

Source: De-Márquez-Farías and Márquez-Romance (2023).

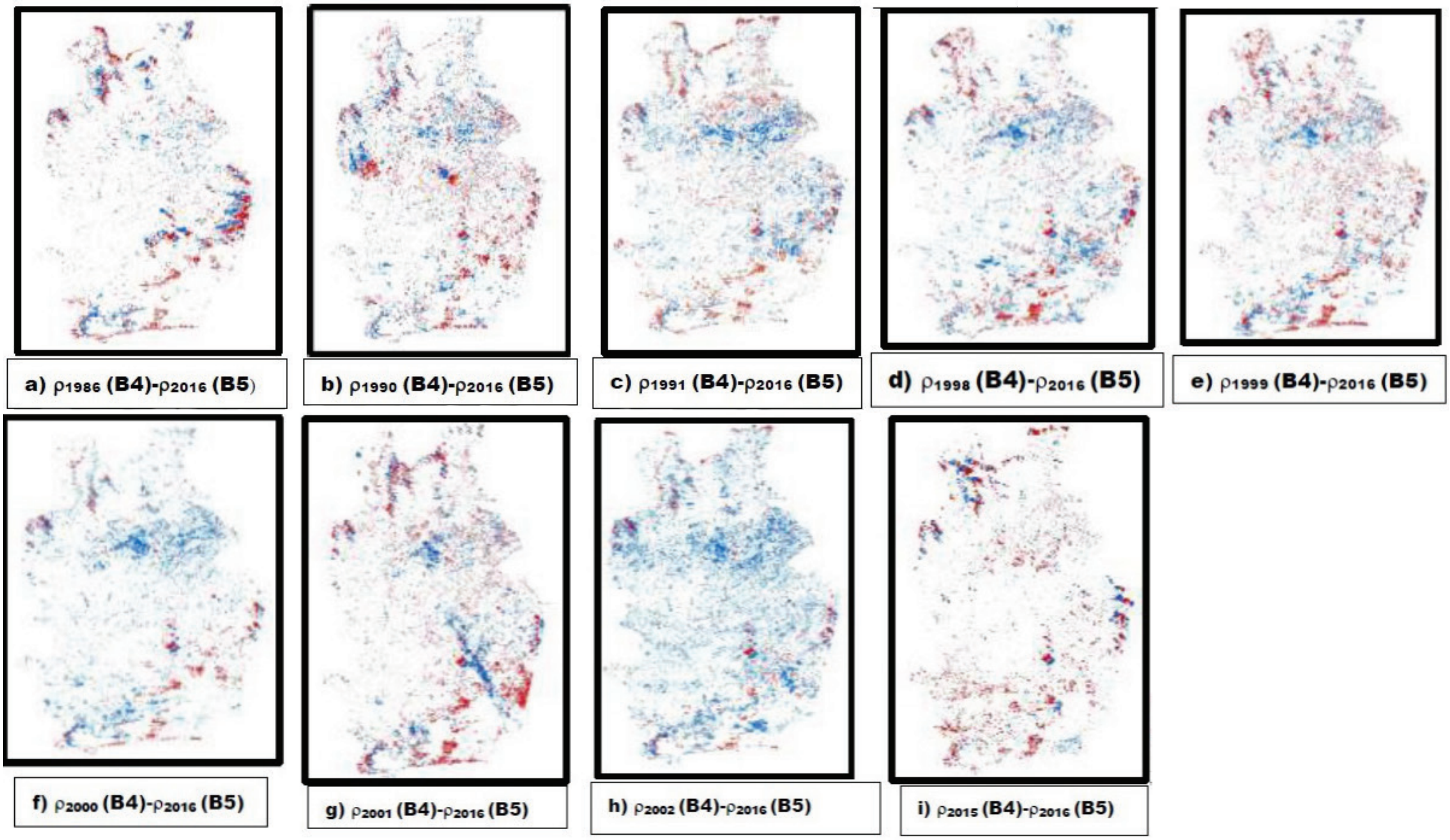
a) ρ_{1986} **(B4)**-ρ_{2016} **(B5)**
b) ρ_{1990} **(B4)**-ρ_{2016} **(B5)**
c) ρ_{1991} **(B4)**-ρ_{2016} **(B5)**
d) ρ_{1998} **(B4)**-ρ_{2016} **(B5)**
e) ρ_{1999} **(B4)**-ρ_{2016} **(B5)**
f) ρ_{2000} **(B4)**-ρ_{2016} **(B5)**
g) ρ_{2001} **(B4)**-ρ_{2016} **(B5)**
h) ρ_{2002} **(B4)**-ρ_{2016} **(B5)**
i) ρ_{2015} **(B4)**-ρ_{2016} **(B5)**

Figure 5. Results of the bitemporal reflectance difference image method in the Pao River basin 1986-2016. Spectral band 4 (B4) corresponding to the near-infrared spectral region is the one selected in the reflectance images from the Landsat 5TM satellites: 1986, 1990, 1991, 1998, 1999, 2001 and 7 ETM: 2000, 2002, 2003. Spectral band 5 (B5) corresponding to the near-infrared spectral region is the one used from the reflectance images from the Landsat 8OLI satellite. Source: De-Márquez-Farías and Márquez-Romance (2023).

Results of the reflectance image regression method

The results of the linear regression method of the bitemporal reflectance images (%) in the Pao River, period 1986-2016, related to the parameters a, b, r and the correlation coefficient are shown in Table 8. The correlation coefficient ranged between 0.46 and 0.64, with a high degree of correlation (De-Márquez-Farías & Márquez-Romance, 2023).

Table 8. Results of the linear regression method of bitemporal reflectance images (%) in the Pao River basin from 1986 to 2016.

	1986-2016	**1990-2016**	**1991-2016**	**1998-2016**	**1999-2016**	**2000-2016**	**2001-2016**	**2002-2016**	**2003-2016**	**2015-2016**
a	0.36	0.636	0.51	0.56	0.67	0.44	0.67	0.38	0.39	0.69
b	14.26	8.312	10.97	8.41	7.55	4.97	8.12	5.24	4.18	7.65
r	0.46	0.610	0.52	0.62	0.63	0.64	0.60	0.55	0.62	0.5

The results of applying the regression method to the reflectance images in the Pao River basin over a period of two years, 2000–2016, are shown in Figures 6a and 6b. The first shows 10,500 points generated to extract the reflectance values from the 2000 and 2016 images. In the second, the dispersion of the reflectance sample points in the 2000 image is plotted relative to the 2016 reflectance image (De-Márquez-Farías & Márquez-Romance, 2023).

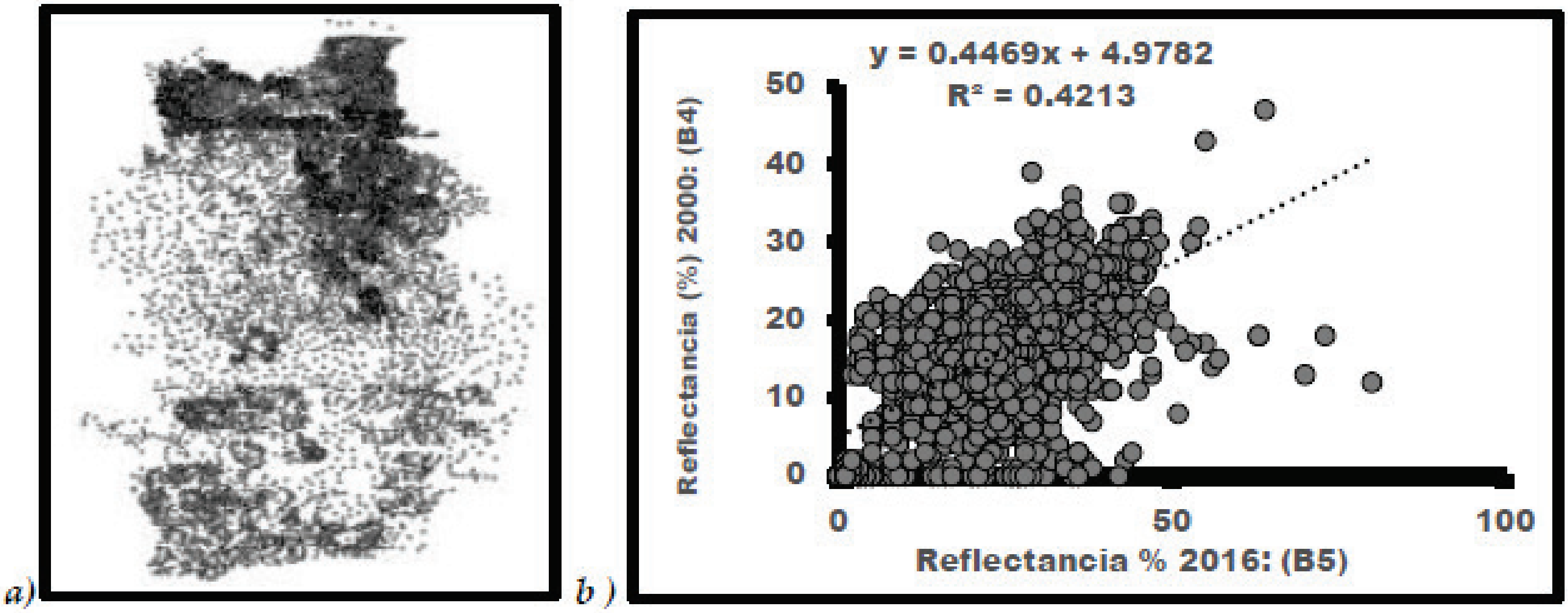

Figure 6. Results of applying the regression method to reflectance images in the Pao River basin bitemporal 2000-2016. Spectral band 4 (B4) corresponding to the near-infrared spectral region is the one selected in the reflectance images from the Landsat 7 ETM: 2000 satellites. Spectral band 5 (B5) corresponding to the near-infrared spectral region is the one used from the 2016 reflectance image of the Landsat 8OLI satellite. Source: De-Márquez-Farías and Márquez-Romance (2023).

These data are fitted to a linear regression mathematical model. The model is represented by the parameters a and b, 0.44 and 4.79, respectively. The coefficient of determination statistic is 0.42, which is equivalent to a regression coefficient of 0.64. According to Guevara and Cartaya (2004), they indicate that the degree of correlation is low and the forecasting capacity is insufficient. The rest of the regression coefficients are less than 0.64, varying between 0.46 and 0.64. The results indicate that the returned image under these conditions excludes atmospheric effects such as clouds and shadows; however, since dispersion is high in the vicinity of the linear model, much of the information is lost through the use of the returned image (De-Márquez-Farías & Márquez-Romance, 2023).

The results of applying the difference for regression method on reflectance images in the Pao River basin bitemporal 2000 (B4) - 2016 (B5) are shown in Figure 7. The components from which the difference image in Figure 7c is generated are: Figure 7a: reflectance (%) in 2000 devoid of clouds and shadows. Figure 7b: reflectance (%) in 2000 regressed and Figure 7c: reflectance (%) in 2016. The results are as follows: 1) there are significant differences between the original and regressed images of 2000. 2) The regressed image of 2000 predominantly reproduces the spatial variation of reflectances observed in the 2016 image, 3) the resulting regressed reflectance difference image 2000 - 2016 is a pattern of the 2016 image; The magnitudes in the 2016 reflectance have been slightly attenuated by the returned 2000 reflectance image; this is evidenced by the negative trend observed in Figure 7c. In summary, the bitemporal reflectance image regression method has proven to be relatively unreliable in obtaining changes in land cover and uses in the Pao River basin (De-Márquez-Farías & Márquez-Romance, 2023).

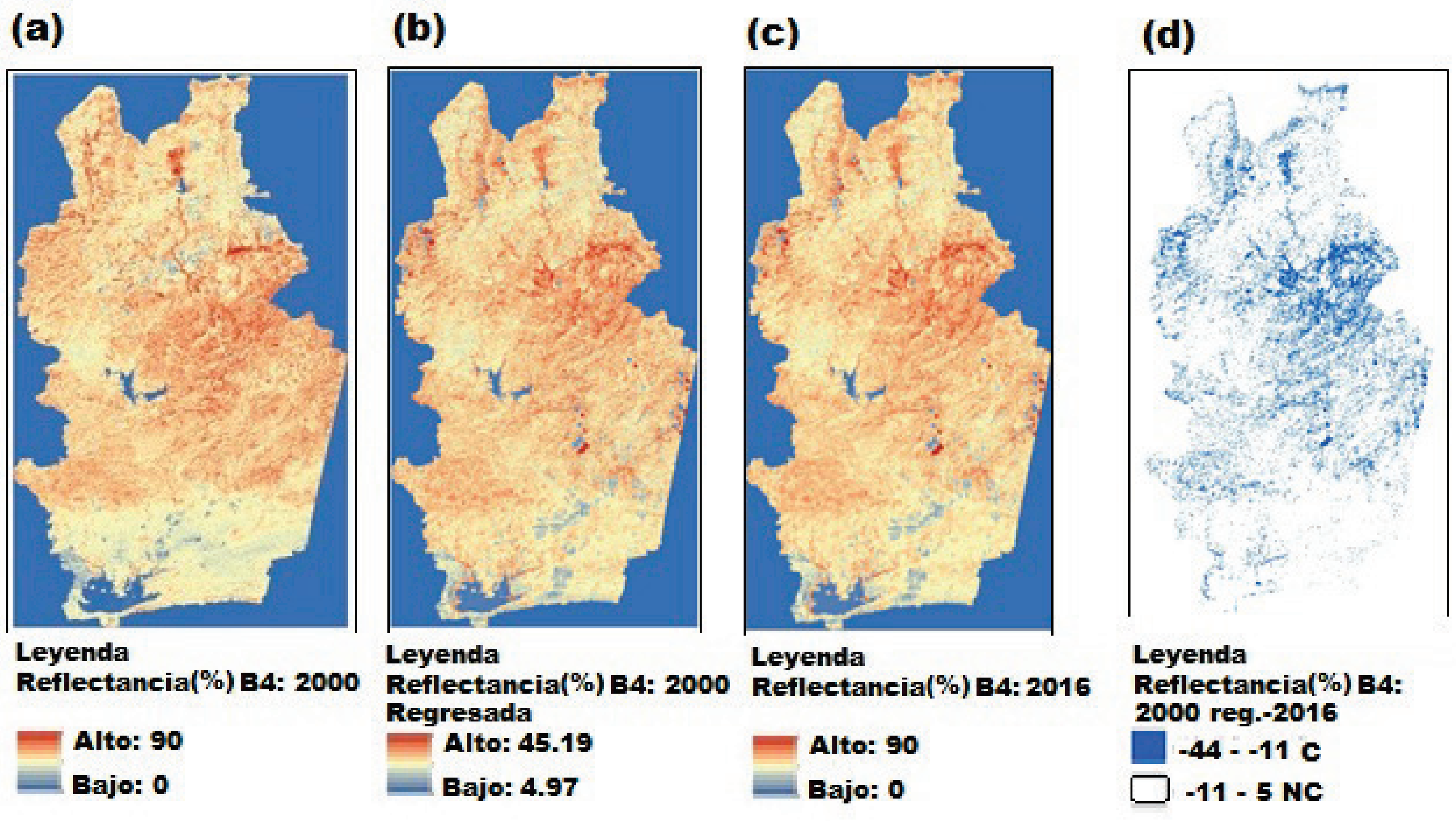

Figure 7. Results of applying the regression method to reflectance images in the Pao River basin in a bitemporal period from 2000 to 2016. Spectral band 4 (B4), corresponding to the near-infrared spectral region, is the one selected in the reflectance images from the Landsat 7 ETM: 2000 satellites. Spectral band 5 (B5), corresponding to the near-infrared spectral region, is the one used in the 2016 reflectance image from the Landsat 8OLI satellite: A) reflectance (%) in 2000; B) reflectance (%) in 2000 regressed; C) reflectance (%) in 2016; D) difference between reflectance in 2000 and reflectance in 2016. Source: De-Márquez-Farías and Márquez-Romance (2023).

Results of the reflectance image ratio method

The results of the bitemporal image ratio method of reflectance (%) expressed by the proportion of Change/No Change areas in the maps obtained in the Pao River Basin from 1986 to 2016 are shown in Table 9. The areas of change ranged from 0.31 to 2.64 %, while mostly no changes occurred at approximately 97.36 to 99.69 %.

Table 9. Results of the reflectance image ratio method (%) in the Pao River basin from 1986-2016.

	1986-2016	**1990-2016**	**1991-2016**	**1998-2016**	**1999-2016**	**2000-2016**	**2001-2016**	**2002-2016**	**2003-2016**	**2015-2016**
C %	2.64	0.71	0.71	0.89	0.94	0.89	0.75	0.31	0.86	0.86
NC %	97.36	99.29	99.29	99.11	99.06	99.11	99.25	99.69	99.14	99.14

The results of the bitemporal reflectance image ratio method expressed through the classification accuracy error matrix are shown in Table 10, where the overall accuracy index was 38.33 % and the Global Kappa statistic was -0.23 (De-Márquez-Farías & Márquez, 2023).

Table 10. Results of the bitemporal reflectance image ratio method expressed by the error matrix on classification accuracy in the Pao River basin from 1986 to 2016.

Classified data		**Reference data**		**Total classifieds**	**User accuracy (%)**	**K**
		No change	**Increase**			
Reflectance image relationship						
CT/UT classification Map	**No change (NC)**	16	0	16	**100.00**	**1**
	Increase (INC)	74	30	104	**28.85**	**-1.466**
	Totals in the reference	**90**	**30**	**120**		
Producer accuracy (%)		**17.78**	**100**			
Global classification accuracy (%)						**38.33**
Global Kappa Statistics						**-0.23**

Source: De-Márquez-Farías y Márquez-Romance (2023).

The results of applying the % reflectance image ratio method (ρ) in the Pao River basin bitemporally 1986-2016 are shown in Figure 8. Spectral band 4 (B4) corresponding to the near-infrared spectral region is the one selected in the reflectance images of the Landsat 5TM satellites: 1986, 1990, 1991, 1998, 1999, 2001 and Landsat 7ETM: 2000, 2002, 2003. The specific bitemporal reflectance ratio is shown from a to i; where it is generally observed that the images predominantly have areas with a ratio that varies between 1 and 2; which implies that there was no change. The areas where changes occurred show reflectance ratios between 2 and 90. Three land-use and land-cover components are present in these areas: agricultural zones, water bodies, and clouds. Regarding the water body circled in Figure 8, ratios greater than unity occur in areas where it could contain a high proportion of sediment (Figures 8a to 8d); this is justified by the high agricultural use in the watershed surrounding this reservoir in the years prior to 2000, indicated by a box on the maps in Figures 8a to 8i. This high agricultural use leads to high-intensity irrigation use of crops during the dry season. Soils with high humidity decrease reflectance, which could explain the contrast between the reflectance image from years prior to 2016 and the current one. These figures show that agricultural uses could have decreased over time. The decrease in agricultural activity could lead to a reduction in sediment transport to the water body. A decrease in sediment in a water body decreases reflectance. Similarly, incremental eutrophication processes in years after 1999 could equalize reflectance between years after 1999 and 2016; and suppress the contrast in the reflectance ratios for the water body on the maps in Figures 8e to 8i (De-Márquez-Farías & Márquez-Romance, 2023).

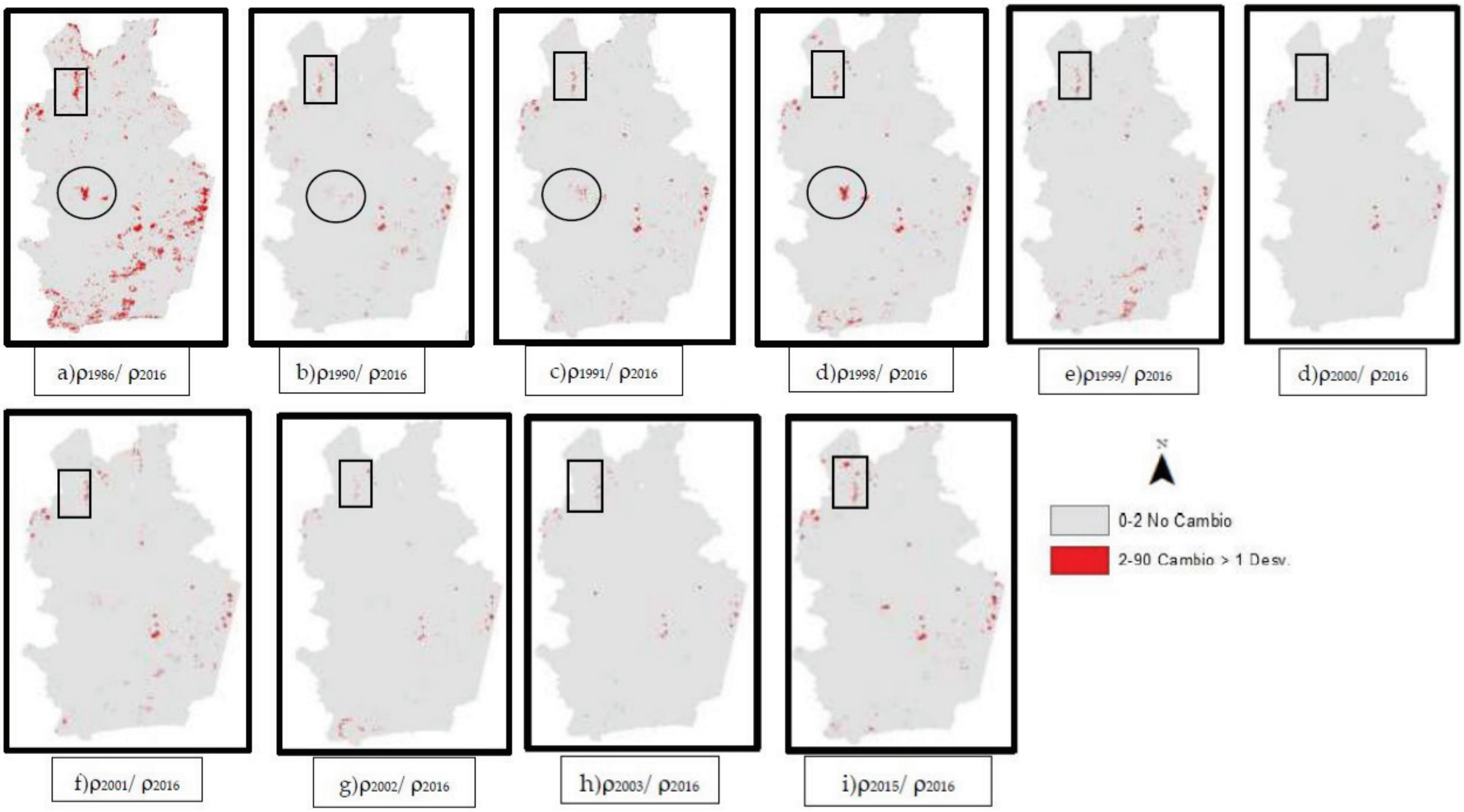

Figure 8. Results of the reflectance ratio method of bitemporal images (ρ) in the Pao River basin 1986-2016. Spectral band 4 (B4) corresponding to the near-infrared spectral region is the one selected in the reflectance images of the Landsat 5TM satellites: 1986, 1990, 1991, 1998, 1999, 2001 and 7 ETM: 2000, 2002, 2003. Spectral band 5 (B5) corresponding to the near-infrared spectral region is the one used from the Landsat 8OLI satellite reflectance images. The specific bitemporal reflectance ratio is shown from a to i. Source: De Márquez-Farías & Márquez-Romance (2023).

Results of the vegetation index image difference method

The results of the difference method of bitemporal NDVI images expressed by the proportion of areas of change/No Change in the Pao River basin, period 1986-2016, are as follows, as a sample (Table 11): 1986-2016: 1.73 %, 98.27 % (De-Márquez-Farías & Márquez-Romance, 2023).

Table 11. Results of the difference method of bitemporal NDVI images expressed by the ratio of Change/No Change areas in the Pao River basin from 1986 to 2016.

Bitemporal Images	**1986-2016**	**1990-2016**	**1991-2016**	**1998-2016**	**1999-2016**	**2000-2016**	**2001-2016**	**2002-2016**	**2003-2016**	**2015-2016**
Percentage Area Ratio: Change	1.73	1.18	1.66	1.57	2.09	3.57	1.71	5.60	5.31	1.82
Percentage Area Ratio: No Change	98.27	98.82	98.34	98.43	97.91	96.43	98.29	94.40	94.69	98.18

Source: De-Márquez-Farías and Márquez-Romance (2023).

The results of the difference method of bitemporal NDVI images expressed through the error matrix in the classification accuracy in the Pao River basin from 1986 to 2016 are shown in Table 12; where the correspondence between the pixels in the classified map (MC) of land covers (CT) and land uses (UT) can be observed. The results of the mathematical operations on pixels in areas with clouds and shadows have been grouped under the category of no change (De-Márquez-Farías & Márquez-Romance, 2023).

Table 12. Results of the bitemporal NDVI image difference method expressed by the error matrix in classification accuracy in the Pao River basin from 1986 to 2016.

Classified data		**Reference Data**			**Total Classifieds**	**User Accuracy (%)**	**K**
		Decrease	**No Change**	**Increase**			
Difference in NDVI Images 1986-2016							
CT/UT Classification Map	**Decrease**	39	2	0	**41**	95.12	0.948
	No Change	0	32	0	**32**	100.00	1
	Increase	0	15	12	**27**	44.44	-0.25
	Totals in the reference	**39**	**49**	**12**	**100**		
Producer Accuracy (%)		100	65.31	100			
Global Classification Accuracy (%)							**83.00**
Global Kappa Statistics							**0.5662**

Source: De-Márquez-Farías and Márquez-Romance (2023).

The results of the difference method of NDVI images in the Pao River basin bitemporal 1986-2016 are shown in Figure 9; where spectral bands 3 (B3) and 4 (B4) of the reflectance corresponding to the red and near-infrared regions are those used for the estimation of NDVI from the Landsat 5TM satellite images: 1986, 1990, 1991, 1998, 1999, 2001 and Landsat 7 ETM: 2000, 2002, 2003. Spectral bands 4 (B4) and 5 (B5) corresponding to the red and near-infrared spectral region are those used for the estimation of NDVI from the Landsat 8OLI satellite reflectance images (De-Márquez-Farías & Márquez-Romance, 2023).

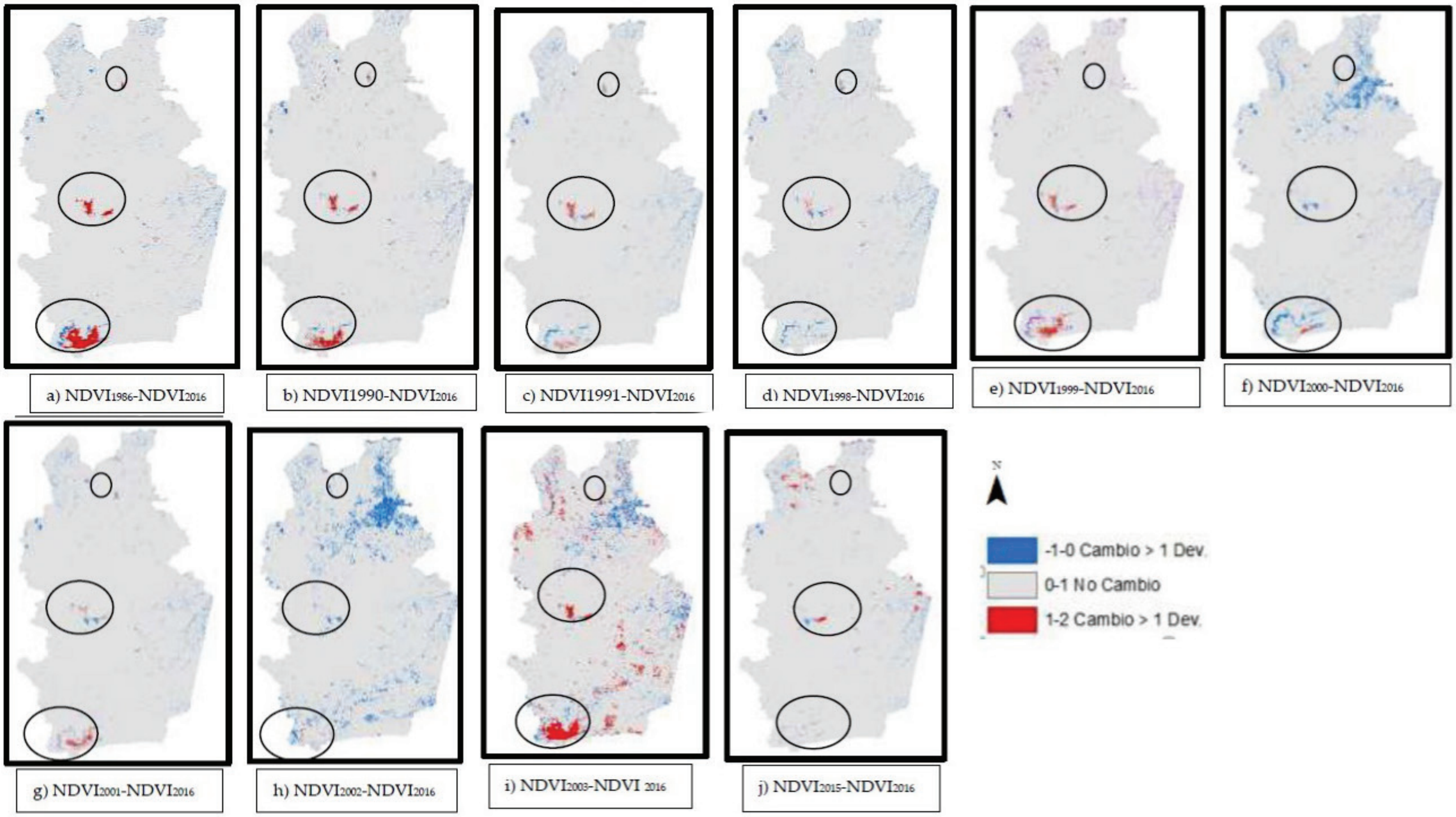

a) NDVI$_{1986}$-NDVI$_{2016}$

b) NDVI1990-NDVI$_{2016}$

c) NDVI1991-NDVI$_{2016}$

d) NDVI$_{1998}$-NDVI$_{2016}$

e) NDVI$_{1999}$-NDVI$_{2016}$

f) NDVI$_{2000}$-NDVI$_{2016}$

g) NDVI$_{2001}$-NDVI$_{2016}$

h) NDVI$_{2002}$-NDVI$_{2016}$

i) NDVI$_{2003}$-NDVI $_{2016}$

j) NDVI$_{2015}$-NDVI$_{2016}$

Figure 9. Results of the difference method of NDVI images in the Pao River basin bitemporal 1986-2016. Spectral bands 3 (B3) and 4 (B4) of reflectance corresponding to the red and near-infrared regions are those used for the estimation of NDVI from the Landsat 5TM satellite images: 1986, 1990, 1991, 1998, 1999, 2001 and Landsat 7 ETM: 2000, 2002, 2003. Spectral bands 4 (B4) and 5 (B5) corresponding to the red and near-infrared spectral region are those used for the estimation of NDVI from the Landsat 8OLI satellite reflectance images. Source: De-Márquez-Farías and Márquez-Romance (2023).

The specific bitemporal NDVI difference from a to j shows: 1) similar NDVI values on date 1 and date 2; resulting in differences that vary predominantly between 0 and 1; which implies areas where there was no bitemporal change. 2) positive values that vary between 1 and 2 mainly in the three water bodies or reservoirs that make up the Pao River basin (De-Márquez-Farías & Márquez-Romance, 2023). The positive values are associated with the 2016 NDVI; which is a value with a negative sign and an approximately zero value of the NDVI in the images from dates prior to 2016. The negative sign value is due to the fact that the reflectance in the spectral band of the red spectral region (B4) is higher than the reflectance in the spectral band of the near-infrared spectral region (B5). 3) The negative NDVI difference values are due to negative NDVI values between 1986 and 2003, with the NDVI value in 2016 being approximately zero. The areas where this occurs correspond to urban uses and wetlands close to the three bodies of water. In the first, the associated material is concrete, and in the second, organic components such as phytoplankton; whose spectral profile shows that the reflectance in spectral band 3 (B3) is greater than the reflectance in spectral band 4 (B4) of the Landsat 5TM and 7ETM images (Bukata, Jerome, Kondratyev, Pozdnyakov, & Kotykhov, 1997; Han & Rundquist, 1997; Giri, Zhu, & Reed, 2005; Jensen, 2009).

Results of the change vector analysis method on reflectance images

The results of this method are shown below in Table 13 (De-Márquez-Farías & Márquez-Romance, 2023), where the largest angles generated from the linear relationship between the reflectance in spectral band 4 versus the reflectance in spectral band 3 were obtained for the years

1986, 2001 and 2015, allowing us to assume scenes of the Pao River basin with more vegetation compared to other uses and years.

Table 13. Results of the change vector method in the Pao River basin from 1986-2016. The method parameters are generated from the linear relationship between reflectance in spectral band 4 vs. reflectance in spectral band 3 in Landsat 5TM and 7ETM images as follows: the angle on date 1 the angle on **date** 2 and the difference in angles between date 1 and date 2.

Bitemporal Images		**1986-2016**	**1990-2016**	**1991-2016**	**1998-2016**	**1999-2016**	**2000-2016**	**2001-2016**	**2002-2016**	**2003-2016**	**2015-2016**
Vector of Change	θ_1	30.8	11.0	10.6	12.3	10.8	2.54	21.6	11.0	10.9	25.7
	θ_{2016}	11.0	11.0	11.0	11.0	11.0	11.0	11.0	11.0	11.0	11.0
	$\Delta\theta$	19.8	0.01	-0.32	1.31	-0.17	-8.46	10.6	0.08	-0.09	14.7

Source: De-Márquez-Farías y Márquez-Romance (2023).

Figure 10 and Figure 11 show the results of the change vector method on reflectance images in the Pao River basin bitemporal 1986-2016 (De-Márquez-Farías & Márquez-Romance, 2023). Spectral bands 3 (B3) and 4 (B4) of reflectance corresponding to the red and near-infrared regions are used to estimate reflectance from Landsat 5TM satellite images: 1986, 1990, 1991, 1998, 1999, 2001 and Landsat 7 ETM: 2000, 2002, 2003. Spectral bands 4 (B4) and 5 (B5) corresponding to the red and near-infrared spectral region are used to estimate reflectance values from Landsat 8OLI satellite reflectance images. The linear model is shown from a to l. Figures 10a and 10b show the dispersion of the reflectance values independently; being increasing and linear. Figure 10c shows the result of superimposing Figures 10a and 10b (De-Márquez-Farías & Márquez-Romance, 2023).

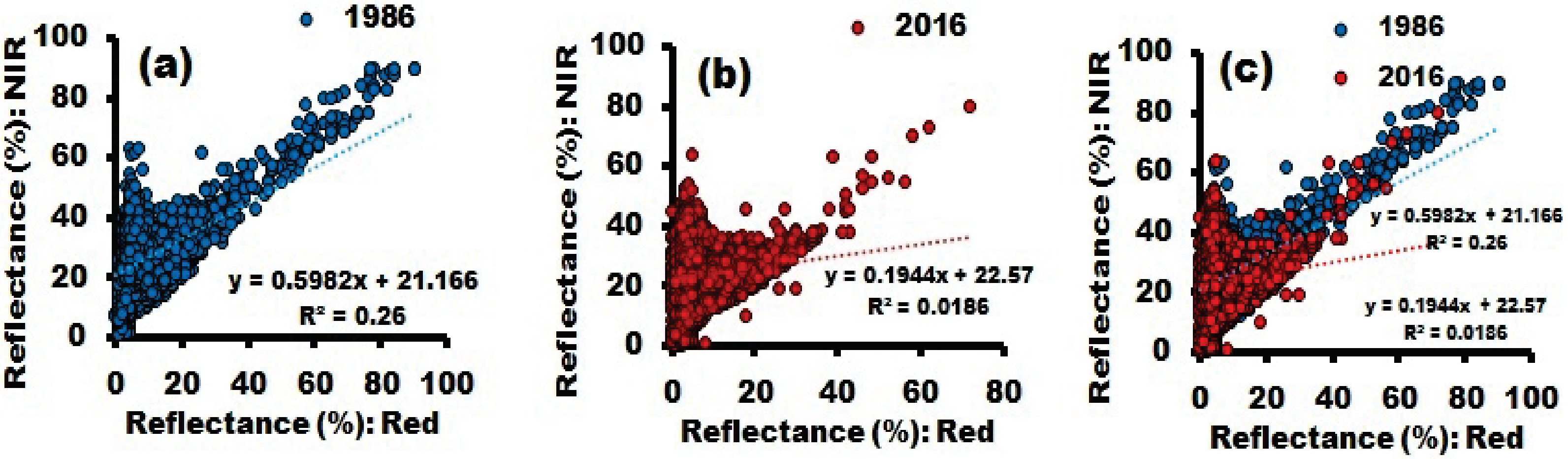

Figure 10. Results of the shift vector method expressed as the difference in the angles of inclination and distance between vectors derived from information on parameters of linear model fitting to reflectance observations in the Pao River basin from bitemporal images in the period 1986-2016. Source: De-Márquez-Farías and Márquez-Romance (2023).

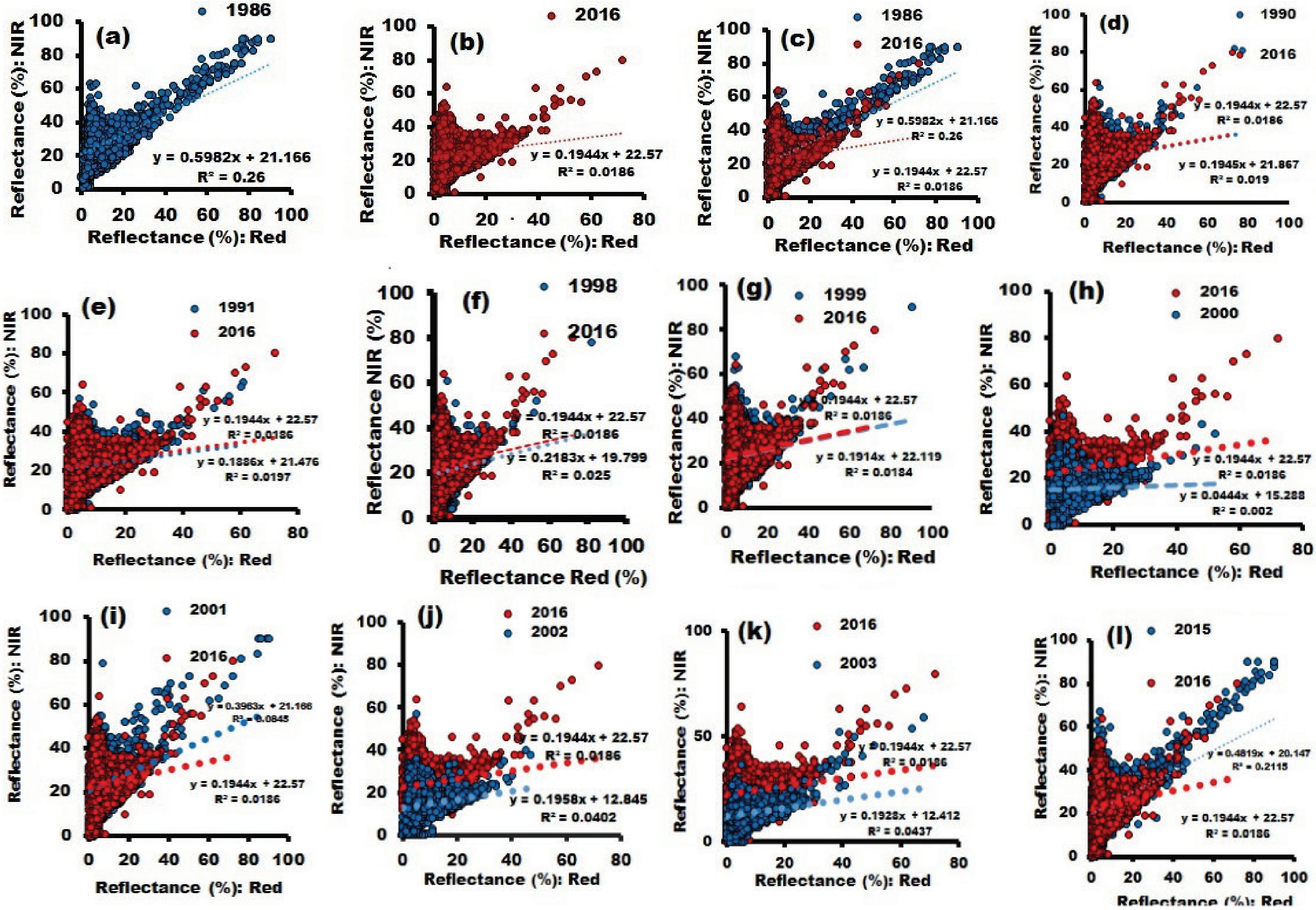

Figure 11. Results of the change vector method expressed as the difference in the angles of inclination and distance between vectors derived from information on parameters of linear model fitting to reflectance observations in the Pao River basin from bitemporal images in the period 1986-2016. Source: De-Márquez-Farías and Márquez-Romance (2023).

The trends shown in Figures 11a, 11b, and 11c are similar to those observed in Figures 11d through 11l. The linear patterns found for each bitemporal image set are based on the parameters a, b, and the statistic r. Significant differences between the direction angles of each reflectance data set are found among the information extracted from the following bitemporal images: 1986–2016: 19.89°, 2001–2016: 10.62°, and 2015–2016: 14.73°. This significant change could be due to the occurrence of: 1) high vegetation cover from one year to the next; which increases the reflectance as is the case of 2000-2016, high presence of clouds and shadows as is the case of 1986-2016, 2001-2016, 2015-2016 (De-Márquez-Farías & Márquez-Romance, 2023).

Spectral bands 3 (B3) and 4 (B4) of reflectance corresponding to the red and near-infrared regions are used to extract reflectance values from Landsat 5TM satellite images: 1986, 1990, 1991, 1998, 1999, 2001 and Landsat 7 ETM: 2000, 2002, 2003. Spectral bands 4 (B4) and 5 (B5) corresponding to the red and near-infrared spectral region are used to estimate NDVI from Landsat 8OLI satellite reflectance images. The linear model is shown in Figures 11a to 11l (De-Márquez-Farías & Márquez-Romance, 2023).

Results of transformation methods

Results of the transformation method based on the principal components

Principal components are defined in this study as the set of orthogonal linear combinations of reflectance across spectral bands 1–6 that have the maximum variance. The Landsat 5TM reflectance image is composed of six spectral bands corresponding to six regions of the electromagnetic spectrum as follows: Spectral band 1: 0.452–0.518 μm. Spectral band 2: 0.528–0.609 μm. Spectral band 3: 0.626–0.693 μm. Spectral band 4: 0.776–0.904 μm. Spectral band 5: 1,567 – 1,784 μm and Spectral band 7: 2,097 – 2,349 μm (De-Márquez-Farías & Márquez-Romance, 2023).

The purpose of determining the principal components is to reduce the dimensionality of the reflectance variable contained in six spectral bands to one or two components before applying land use and land cover change detection techniques to them in the Pao River basin. The coefficient vectors expressed as covariances or correlation of the six principal components obtained from the linear combination of the six variables represented by the reflectance in each of the six spectral bands of the Landsat 5TM image are contained in Table 14 (De-Márquez-Farías & Márquez-Romance, 2023).

Table 14. Results of the principal components transformation method expressed through the covariance and correlation matrix of the reflectance image (%) 1986 in the Pao River basin.

	Principal component					
	1	**2**	**3**	**4**	**5**	**6**
Covariance						
Spectral band 1	31.46	36.53	34.75	52.42	52.02	41.81
Spectral band 2	36.53	44.75	42.31	69.37	67.38	52.04
Spectral band 3	34.75	42.31	41.53	58.83	62.70	50.47
Spectral band 4	52.42	69.37	58.83	191.36	149.65	90.79
Spectral band 5	52.02	67.38	62.70	149.65	147.89	98.64
Correlation						
Spectral band 1	1.00	0.97	0.96	0.67	0.76	0.86
Spectral band 2	0.97	1.00	0.98	0.74	0.82	0.90
Spectral band 3	0.96	0.98	1.00	0.65	0.80	0.91
Spectral band 4	0.67	0.74	0.65	1.00	0.88	0.76
Spectral band 5	0.76	0.82	0.80	0.88	1.00	0.94
Spectral band 7	0.86	0.90	0.91	0.76	0.94	1.00

Source: De-Márquez-Farías y Márquez-Romance, 2023.

The results of the principal component-based transformation method expressed as the difference of principal component No. 1 based on bitemporal reflectance images as a proportion of Change/No Change areas in the Pao River basin, period 1986-2016, are shown in Table 15 (De-Márquez-Farías & Márquez-Romance, 2023).

Table 15. Results of the principal component-based transformation method expressed as the difference of principal component No. 1 based on bitemporal reflectance images as a proportion of Change/No Change areas in the Pao River basin from 1986-2016.

	1986-2016	**1990-2016**	**1991-2016**	**1998-2016**	**1999-2016**	**2000-2016**	**2001-2016**	**2003-2016**	**2015-2016**
Change %	8.41	13.49	6.43	6.98	7.03	5.43	6.*95*	4.80	3.80
No Change %	91.59	86.51	93.57	93.02	92.97	94.57	93.05	95.20	96.20

Figure 12 and Figure 13 show the results of the principal components transformation method, expressed as the difference of principal component No. 1 based on bitemporal reflectance images as a proportion of Change/No Change areas. The red areas represent a decrease in vegetated areas and areas with cloud occurrences. The blue areas represent increases in urban uses and organic and inorganic compounds in water bodies (De-Márquez-Farías & Márquez-Romance, 2023).

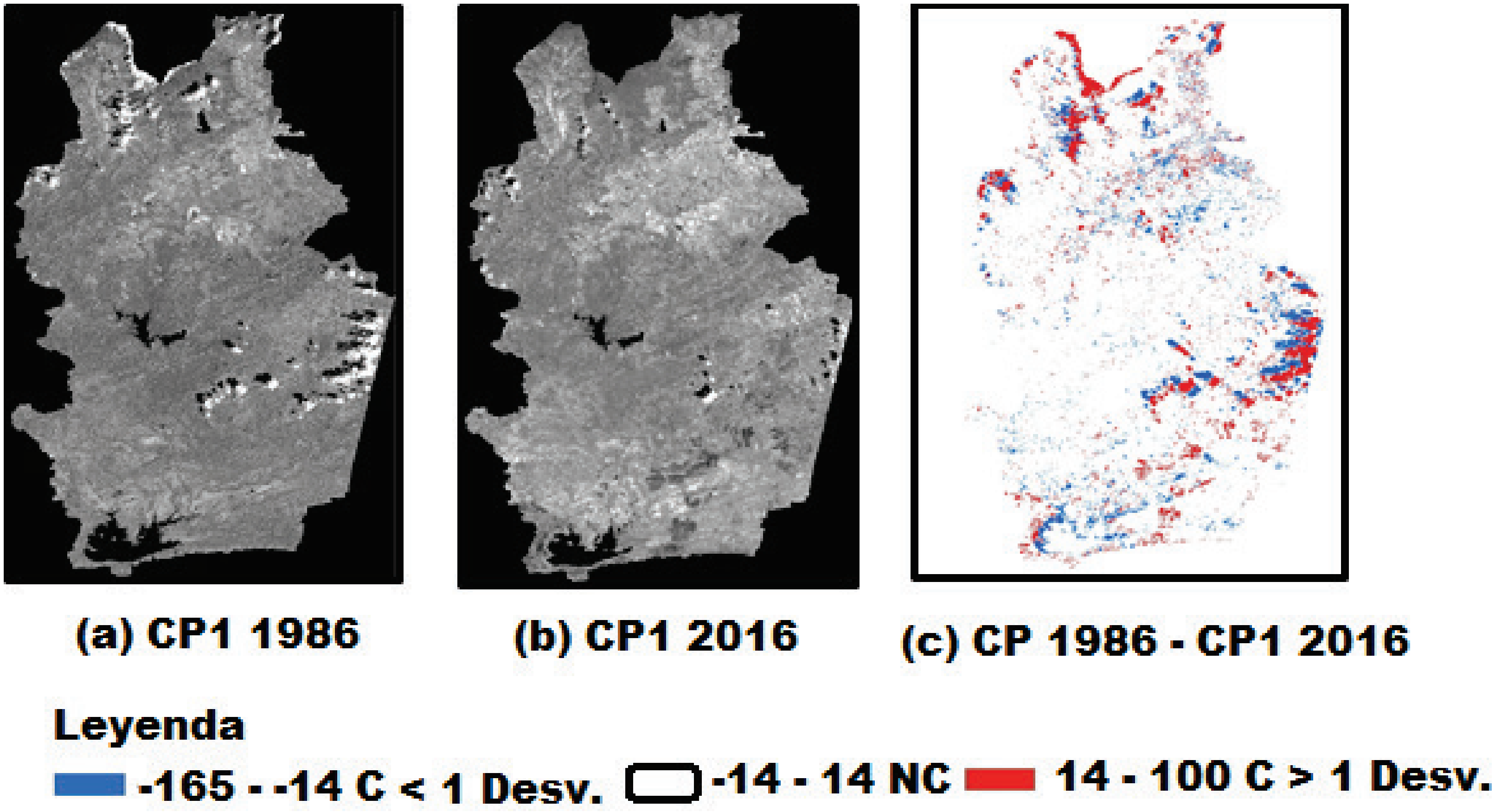

Figure 12. Results of the principal components transformation method expressed as the difference of the principal component No. 1 based on bitemporal reflectance images as a proportion of Change/No Change areas in the Pao River basin from 1986 to 2016. a) Principal component No. 1 derived from the reflectance image in 1986. b) Principal component No. 1 derived from the reflectance image in 2016. c) Difference of the bitemporal principal component No. 1 2016-1986. Source: De Márquez-Farías & Márquez-Romance (2023).

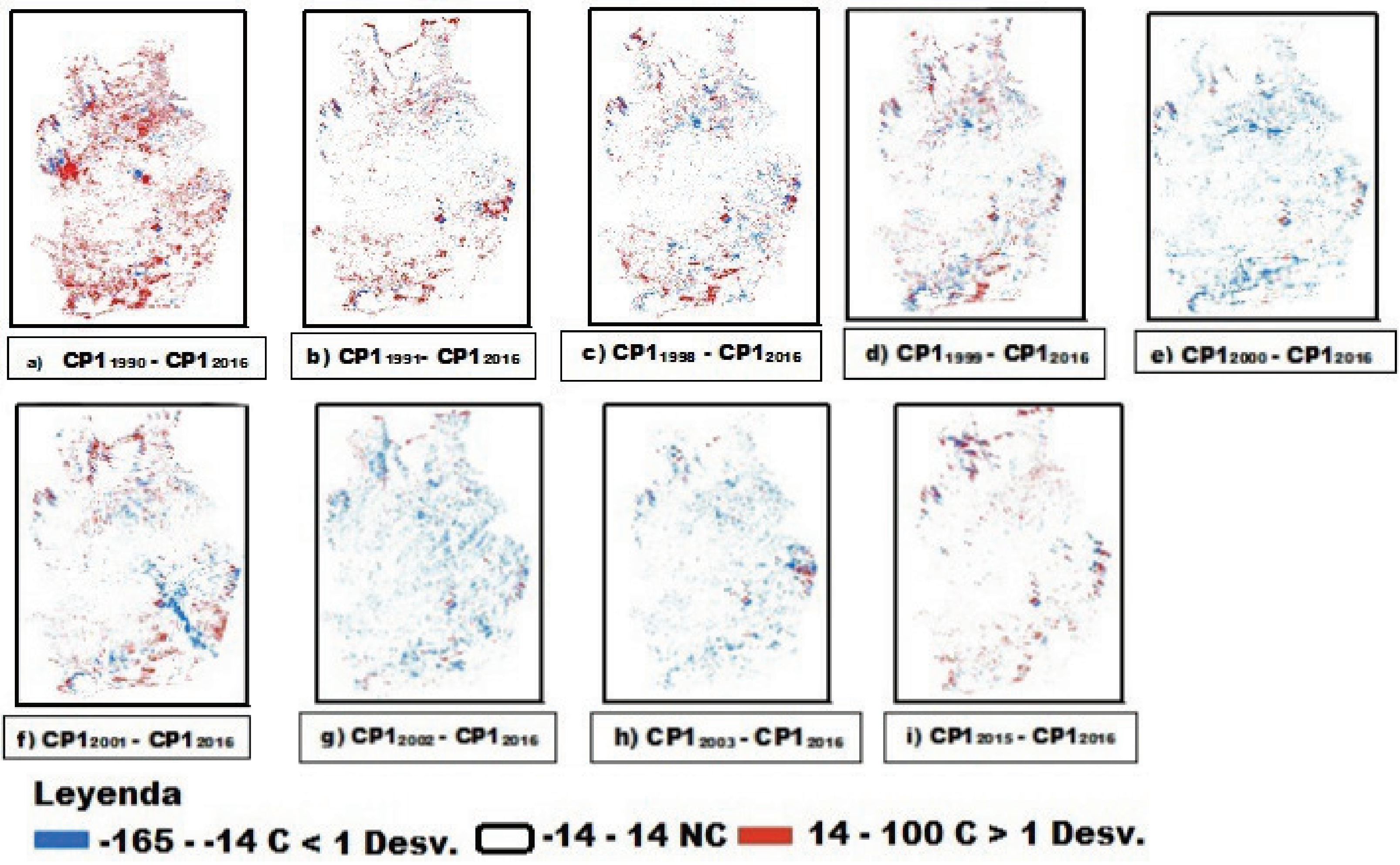

Figure 13. Results of the principal components transformation method expressed as the difference of principal component No. 1 based on bitemporal reflectance images as a proportion of Change/No Change areas in the Pao River basin from 1986-2016. Source: De-Márquez-Farías and Márquez-Romance (2023).

Table 16 and Figure 14 show the results of the bitemporal Principal Component No. 1 image difference method expressed through the classification accuracy error matrix in the Pao River basin from 1986 to 2016, where the following correspondence is observed between the pixels in the classified map (MC) of land covers (CT) and land uses (UT) under the following three categories: Decrease (DIS), No Change (NC) and Increase (INC) and the reference data (DR) based on the corrected images of Landsat 5TM, Landsat 8OLI and Google Earth associated with these three categories for a sample of 891 points: 1) DIS in MC corresponding to DIS in DR: 352, DIS in MC corresponding to NC in DR: 85, DIS in MC corresponding to INC in DR: 0. The global accuracy and Kappa indices are: 84.4 % and 0.872, respectively. Table 14 also shows the results of the error matrices of the following methods (De-Márquez-Farías & Márquez-Romance, 2023): 1) difference of bitemporal brightness index images based on digital number, 2) difference of bitemporal brightness index images based on reflectance images, 3) difference of Principal Component No. 1 images based on bitemporal brightness and greenness index images in the Pao River basin from 1986 to 2000, where the following correspondence is observed between the pixels in the classified map (MC) of land covers (CT) and land uses (UT) under the following three categories: Decrease (DIS), No Change (NC), and Increase (INC), and the reference data (DR) based on the corrected Landsat 5TM and 7ETM images associated with these three categories for a sample of 100, 103, and 100. points, respectively. The results of mathematical operations on pixels in areas with clouds and shadows have been grouped under the category of no change (Figure 14) (De-Márquez-Farías & Márquez-Romance, 2023).

Table 16. 1) Results of the difference method of bitemporal images of the Principal Component No. 1 expressed by the error matrix in the classification accuracy in the Pao River basin from 1986 to 2016; 2) Results of the difference method of bitemporal images of brightness index; 3) Difference of Brightness Index Images based on Reflectance Images: 1986 - 2000; 4) Difference of CP1 images based on images of brightness and greenness index 1986-2000.

Classified data		**Reference data (DR)**			**Total classifieds**	**User accuracy (%)**	**K**
		DIS	**NC**	**INC**			
1. Difference in CP1 Images 1986-2016							
CT/UT classification map	**DIS**	352	85	0	437	**80.55**	**0.758**
	NC	0	20	0	20	**100**	**1**
	INC	0	54	380	434	**87.56**	**0.857**
	Totals in the reference	**352**	**159**	**380**	**891**		
	Producer accuracy (%)	**100**	**12.58**	**100**			
Global classification accuracy (%)							**84.4**
Global Kappa statistics							**0.872**
2. Difference of brightness index images based on digital number images: 1986-2000							
CT/UT classification map	**DIS**	51	14	0	65	**78.46**	**0.725**
	NC	0	8	0	8	**100**	**1**
	INC	0	1	26	27	**96.3**	**0.961**
	Totals in the reference	**51**	**23**	**26**	**100**		
	Producer accuracy (%)	**100**	**34.78**	**100**			
Global classification accuracy (%)							**85**
Global Kappa statistics							**0.895**

Classified data		Reference data (DR)			Total classifieds	User accuracy (%)	K
		DIS	NC	INC			
3. Difference of brightness index images based on reflectance images: 1986 - 2000							
CT/UT classification map	**DIS**	31	15	0	**46**	**67.39**	**0.516**
	NC	0	3	0	**3**	**100**	**1**
	INC	0	14	40	**54**	**74.07**	**0.65**
	Totals in the reference	**31**	**32**	**40**	**103**		
	Producer Accuracy (%)	**100**	**9.38**	**100**			
Global classification accuracy (%)							**71.84**
Global Kappa statistics							**0.722**
4. CP 1 Image difference based on brightness and greenness index images: 1986 - 2000							
CT/UT classification map	**DIS**	26	2	0	28	**92.86**	**0.923**
	NC	0	5	0	5	**100**	**1**
	INC	0	7	60	67	**89.55**	**0.983**
	Totals in the reference	**26**	**14**	**60**	**100**		
	Producer Accuracy (%)	**100**	**35.71**	**100**			
Global classification accuracy (%)							**91**
Global Kappa statistics							**0.968**

Source: De-Márquez-Farías and Márquez-Romance, 2023.

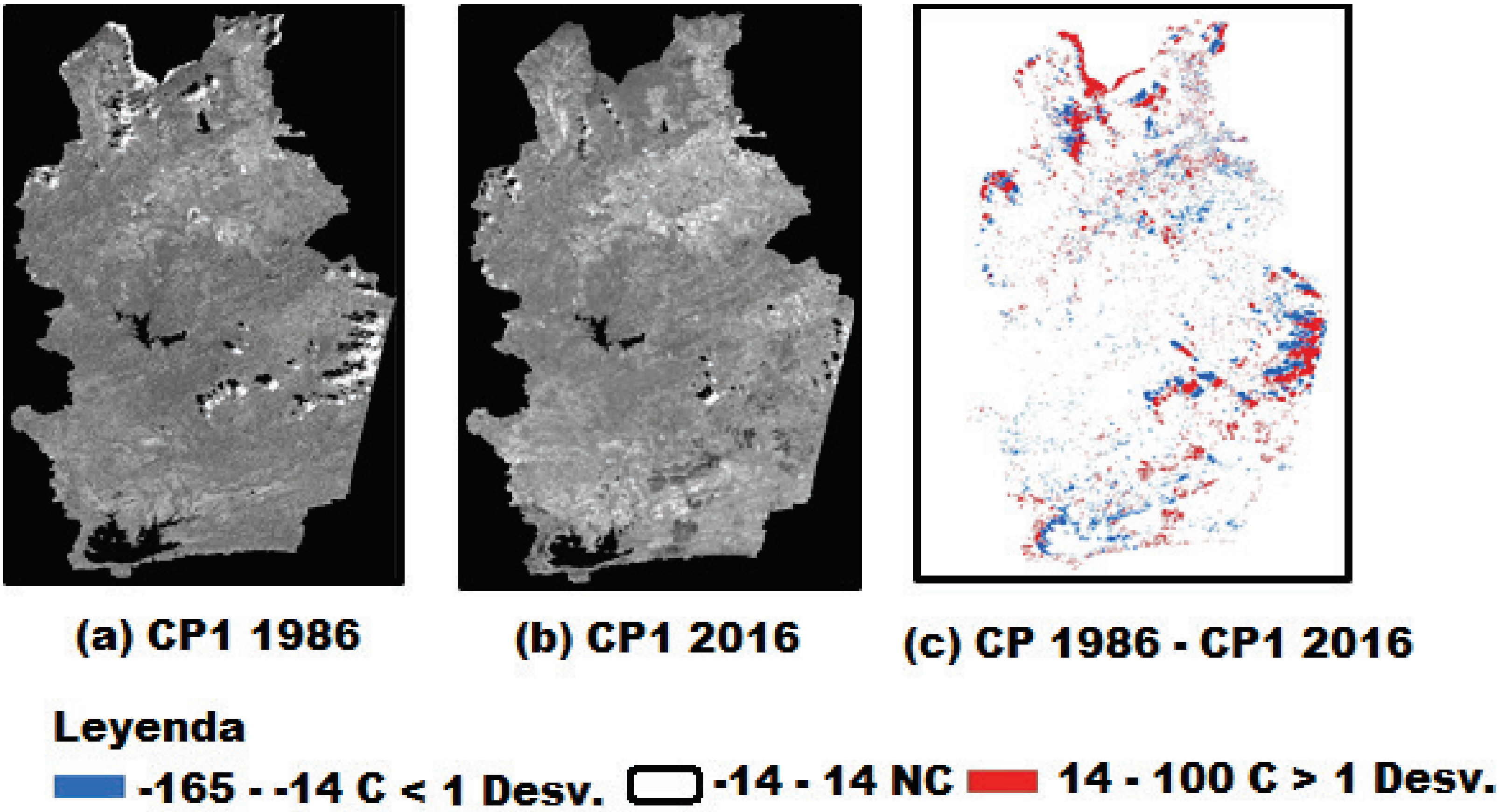

Figure 14. Results of the principal components transformation method expressed as the difference of the principal component No. 1 based on bitemporal reflectance images as a proportion of Change/No Change areas in the Pao River basin from 1986 to 2016. a) Principal component No. 1 derived from the reflectance image in 1986. b) Principal component No. 1 derived from the reflectance image in 2016. c) Difference of the bitemporal principal component No. 1 2016-1986. Source: De Márquez-Farías & Márquez-Romance (2023).

Results of the Kauth and Thomas transformation method

Figure 15 shows the results of the Kauth-Thomas transformation method expressed as the difference of the Brightness Index based on bitemporal digital number images 1986-2 000 as a proportion of Change/No Change areas in the Pao River basin; where three aspects are observed (De-Márquez-Farías & Márquez-Romance, 2023): 1) negative values of the brightness index correspond to areas where there have been increases in bitemporal vegetation cover represented in blue, 2) values close to zero are equivalent to areas where no bitemporal change has occurred in land cover and uses, and 3) positive values are equivalent to areas where the brightness index of the image before 2016 and the 2016 image has decreased; meaning a possible increase in urban and agricultural use; which becomes more evident in the bitemporal differences 1986-2016 and 1990-2016 (De-Márquez-Farías & Márquez-Romance, 2023).

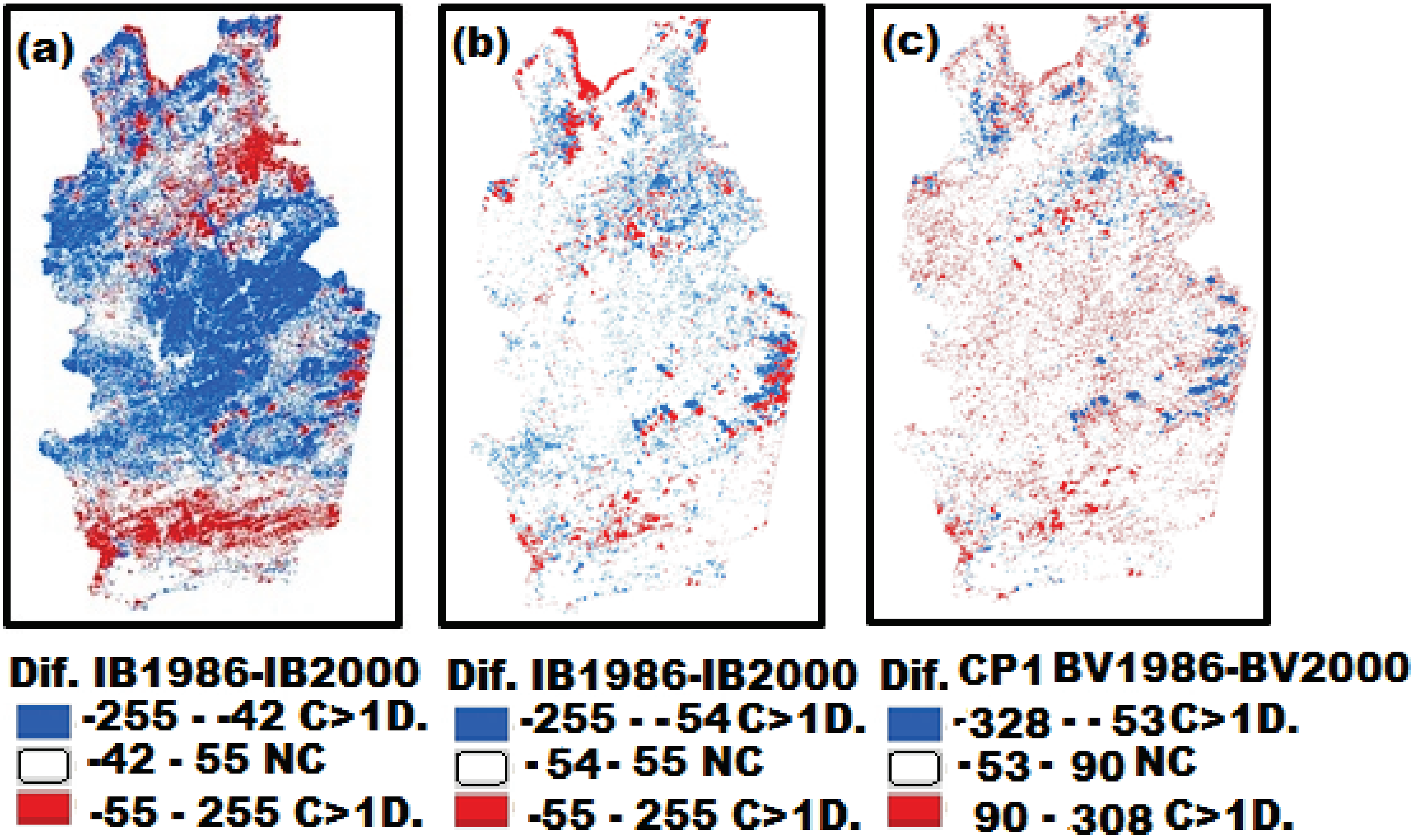

Figure 15. Results of the Kauth-Thomas transform method expressed as: a) Difference in Brightness Index based on Digital Number images: 1986 - 2000, b) Difference in Brightness Index based on Reflectance images: 1986-2000 and c) Difference in Principal Component No. 1 based on Brightness and Greenness images: 1986-2000. Figures 15a to 15c show the areas of Change/No Change in the Pao River basin from 1986-2000. Source: De Márquez-Farías & Márquez-Romance (2023).

Discussion

As a sample, Figure 16 presents the percentages of the change area according to each change detection method of the pre-classification type, varying in a range as follows: a) reflectance image difference: 7 to 10 %; b) reflectance image ratio: 0.5 to 3 %; c) NDVI image difference: 1 to 4 %, and d) principal component image difference: 4 to 10 %.

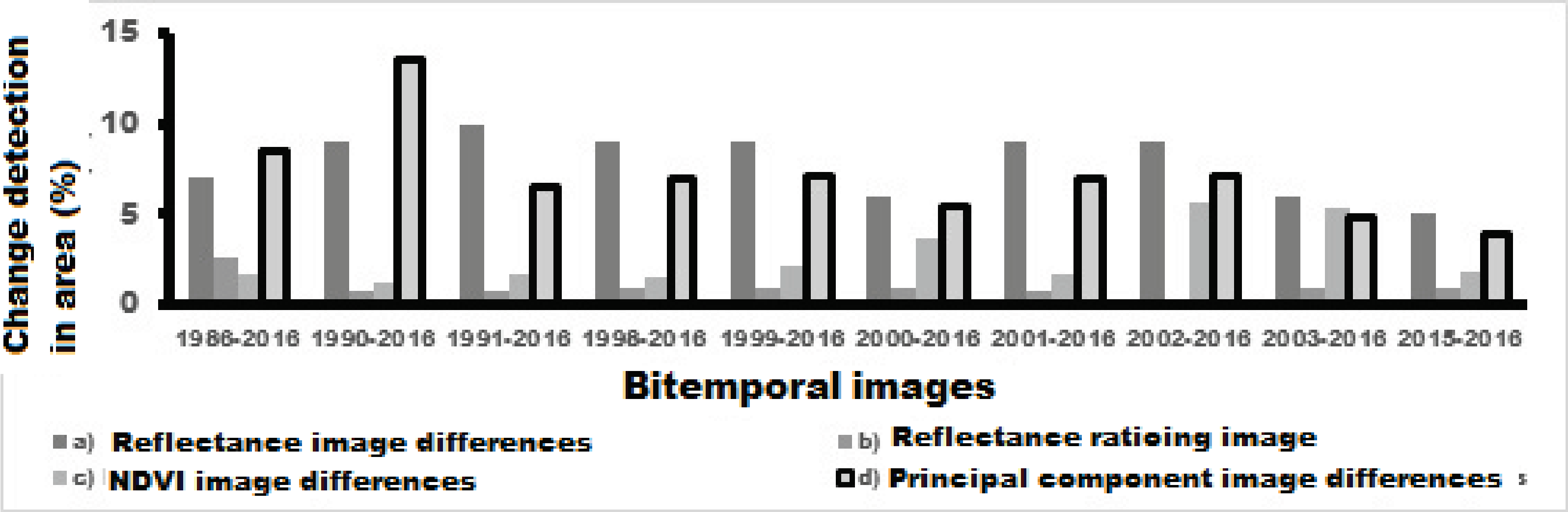

Figure 16. Comparison of the results represented by the area change detection methods based on pre-classification expressed by the percentage of area change: a) Reflectance image difference, b) Reflectance image ratio, c) NDVI image difference and d) Principal component image difference. Source: Prepared by the authors.

Figure 17 and Figure 18 show that the Kappa and overall accuracy coefficients ranged from 0.6 to 0.8, with acceptable classification of areas of change and areas of no change. Figures 18 and 19 also show that the post-classification method using the maximum likelihood (ML) algorithm was slightly higher in classification accuracy than the pre-classification methods. The lowest rates were found for the reflectance image ratio method. This is because the proportion of the sample corresponding to change points is lower than the occurrence of no-change points. The rest of the post-classification and pre-classification methods provide similarities in accuracy rates. Foody and Mathur (2004) used the SVM algorithm with a small number of intelligently selected training samples that can be used to classify a data set as accurately as a larger, conventionally derived training set. The results illustrate the potential of targeting training data acquisition strategies to identify the most useful training samples, enabling efficient and accurate image classification. Otukei and Blaschke (2010) performed land cover change assessment using pixel-based classification algorithms, including maximum likelihood classifier (MLC), support vector machines (SVM), and decision trees (DTs). DT results were compared with those obtained using SVM and MLC. Overall, acceptable accuracies above 85 % were obtained in all cases.

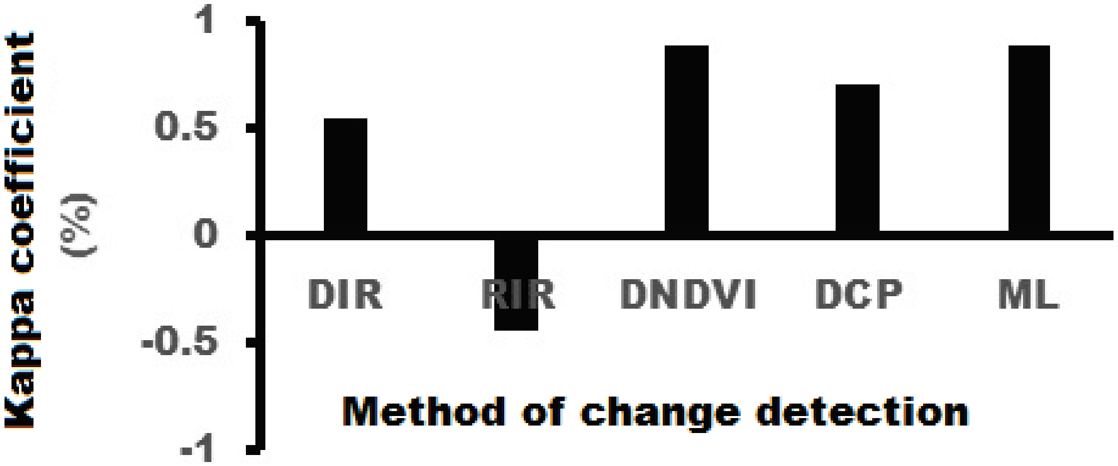

Figure 17. Comparison of results using the kappa coefficient representation found in the change detection methods: Pre-classification: DIR: Difference in Relevance Image; IR: Reflectance Image Ratio; DNDVI: Difference in Normalized Difference Vegetation Index; DCP: Principal Component Difference; Post-classification: ML: Maximum Likelihood.

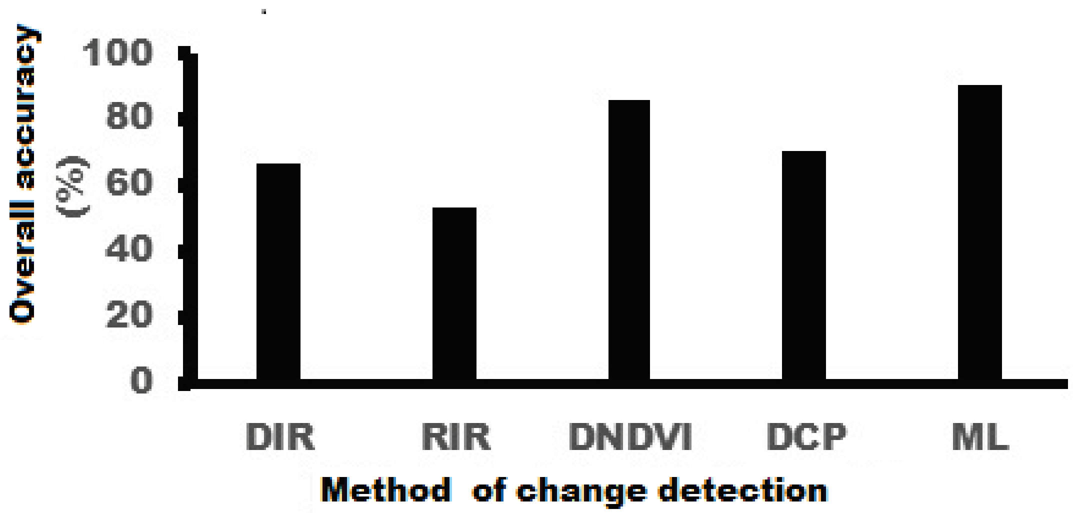

Figure 18. Comparison of results by representing the overall accuracy index found in the change detection methods: Pre-classification: DIR: Difference in Relevance Image; RIR: Reflectance Image Ratio; DNDVI: Difference in Normalized Difference Vegetation Index; DCP: Principal Component Difference; Post-classification: ML: Maximum Likelihood.

Figure 16 shows that the methods whose change estimation is similar are the reflectance image difference and the principal component image difference, as well as the reflectance image ratio and the NDVI difference. In the former case, this is because the reflectance image difference method accounts for reflectance in the near-infrared region, while the principal component image difference, represented by principal component No. 1, includes most of the variance in the visible and infrared regions of the electromagnetic spectrum. The difference between these two methods depends on the land use and land cover within the Pao River basin.

The changes in reflectance detected for the near-infrared region are mainly associated with the following uses and land covers (Figure 5): 1) agricultural, 2) grassland, 3) water, 4) vegetation, 5) clouds, and 6) shadows. This detection of changes is shown in Figure 5, where the areas of decreased reflectance (blue) have been due to changes from vegetated areas to agricultural and livestock uses. In Figure 5, increases in reflectance can also be observed to a lesser extent in agricultural areas, most likely due to the change from agricultural use to vegetation cover, towards the north of the basin and in the vicinity of the Guataparo reservoirs (northern zone), Pao-Cachinche (central zone) and Pao-Las Balsas (southern zone). In this method, the changes from vegetated areas to urban uses that occurred predominantly in the northeastern zone of the basin are largely undetected, being categorized as areas of no change (Figure 5).

Regarding the difference in principal component No. 1, it contains information that includes the change in the six land uses and coverages mentioned above, primarily including urban land use (Figure 14). In the bitemporal differences 1986–2016 and 2003–2016, a pattern is observed in the urban area pixels showing a decrease in reflectance due to the change from vegetation cover to urban land use. For this reason, the area difference in the difference in principal component No. 1 method tends to be greater than the area difference obtained in the image reflectance difference method.

Regarding the image difference methods of reflectance change ratio and NDVI image difference, the area differences are similar because normalization in both methods only allows for change detection when the reflectance change is significant in the bitemporal images. This refers to the change in cover from water to sediment with algae, as is the case in the Guataparo (northern zone), Pao-Cachinche (central zone), and Pao-Las Balsas (southern zone) reservoirs (Figures 9 and 10). This type of temporal change, best appreciated in the near-infrared region, implies that reflectance increases from 3 and 4 % to 30 and 50 %. Sedano, Gong and Ferrao (2005) found that the most consistent results were obtained using principal component analysis of band-pair difference images. This method provided the most accurate classifications for agriculture, wetlands, grasslands, shrublands, and open forest. The overall classification accuracy reached 90 %. Multitemporal NDVI provided more accurate classification for the dense forest cover class. Cakir, Khorram and Nelson (2006) compared the results of standardized and unstandardized Principal Components Analysis (PCA) differencing methods and NDVI for change detection and found a 6.8 % increase in urban-related cover types in the Raleigh metropolitan area between 1993 and 1999. The overall accuracy of the change map generated by the PCA method for the Raleigh metropolitan area was 92.5 %, with an overall Kappa value of 0.88.

With respect to pre-classification, the following three methods: image regression (Figure 6 and Figure 7), change vector (Figure 11 and Figure 12) and tasseled cap (figures 10, 11 and 15); which have been discussed in this study, it has been found that: in the first case, the regressed image corresponding to time (t_1) is an estimate of the image at time (t_2); where the reflectance values are slightly reduced. For this reason, it is not suitable to use it in image differentiation to obtain the bi-temporal change between the image regression time (t_1) and the image time (t_2). According to Vogelmann and Rock (1988), the regression technique implies that the spectral properties of a large majority of the pixels have not changed significantly during the time interval.

Regarding the change vector method, it is a complementary method to the pre- and post-classification methods because it is a measure of the magnitude of the direction angle of change and is also a representation of the Embroidered Cap method (Figures 11, 12 and 16). Sohl (1999) cited the change vector method as excellent in providing special qualitative detail on the nature of change. Kontoes (2008) has indicated that its implementation in such fragmented and dynamically changing landscape environments has resulted in qualified and accurate land cover change maps, achieving an overall classification accuracy level of 88-96 %. Kackaerts, Vaesen, Muys and Coppin (2005) combined the change vector method with three other change detection algorithms: standardized differencing, ratio and principal components analysis, finding it to be an indicator of change in the independent categories corresponding to soil, vegetation and moisture characteristics. In the third case, the Tasseled Cap includes brightness and greenness as main variables. In this study, a principal component analysis was applied to these two variables, obtaining results that provide a good approximation of changes associated with land cover such as water, vegetation, shadows, and clouds; but also an overestimation of soil changes, such as in degraded land, grassland, or urban land classes. Collins and Woodcock (1996) found better performance for principal component analysis and a multitemporal model.

Regarding the Kauth-Thomas transform versus the Gramm-Schmidt orthogonalization process for detecting forest canopy change, Huang *et al*. (2002) found that the brightness, greenness, and wetness from the derived transformation together explained over 97 % of the spectral variance for individual scenes used in their study. Figures 16a-c show a common pattern of change, where decreases in reflectance occurred in the northeastern part of the Pao River watershed due to changes from vegetated to urban areas during the period 1986-2000, as well as increases in reflectance near the artificial reservoirs in the Pao River watershed.

The post-classification comparison method resulted in nine classes: a) urban, b) agricultural, c) agricultural, d) water, e) degraded soil, f) vegetation, g) clouds, h) shade, and i) unclassified. User accuracy ranged between 88.89 and 100.00 %. Producer accuracy ranged between 98.25 and 100.00 %. The overall accuracy index and Kappa index corresponding to the classified maps compared to the Google Earth reference image ranged between 93.00 and 99.40 %, 0.96 and 0.99, respectively. Many studies discuss classifications with overall accuracy below the overall target of 85 % based on the review of 25 articles. Just as they have a wide range in the accuracy with which individual classes have been classified (*e.g.*, Trodd, 1995; DeGloria *et al*., 2000; Ung, Lambert, Guidon, & Fournier, 2000). According to Foody (2002), suggested components for establishing accuracy such as: an error matrix and a metric based on the kappa coefficient are not provided and target accuracies are rarely achieved; based on precision levels for all classes and overall accuracy > 85 %. Trodd (1995) found that the average range in producer accuracy of the reviewed classifications was 59.00 %. Landis and Koch (1977) suggest that the Kappa index between 0.81 and 1 indicates a moderate to almost perfect strength of agreement. The accuracy indices of the classification maps in the land uses and land covers of the Pao River basin indicate a satisfactory level obtained from reflectance images of the Landsat 5TM, 7ETM and 8OLI satellites in the period 1986 to 2016. In the post-classification comparison method, the bitemporal difference of the occupied areas according to the class of land uses and land covers expressed in maximum percentage proportion corresponding to the Pao River basin from 1986 to 2016 shows that the classes that present the increases are: urban: 1.37 % and agricultural: 23 %; while those where the decreases occur are the following: agricultural: 4.97 %; water: 0.55 %; vegetation: 8.10 %; deforested soil: 12 % (De-Márquez-Farías & Márquez-Romance, 2023). Regarding urban use, the National Institute of Statistics (INE) (INE, 2014) has recorded a growth from 1990 to 2011 that varies from 21.72 inhabitants/km^2 to 31.95 inhabitants/km^2.

According to the results obtained from the error matrices of the pre-classification methods; these matrices are derived from a sample of the algebraic and transformation operations on bitemporal images such as: Landsat 5TM of 1986 and Landsat 8OLI of 2016 for the first four methods; as well as Landsat 5TM 1986 and 2000 for the fifth method of Kauth and Thomas indicated as follows: 1) difference of reflectance images in the near-infrared spectral band; Spectral band 4 (0.776-0.904 μm) on Landsat 5TM, spectral band 4 (0.772-0.898 μm) on Landsat 7 ETM and spectral band 5 (0.850-0.880 μm) on Landsat 8 OLI, 2) ratio of reflectance images, 3) difference of vegetation index NDVI, 4) difference of principal component No. 1 based on reflectance image of each year, and 5) difference of brightness index obtained from Kauth and Thomas method it is found that:

1. The global accuracy and Kappa indices obtained are (De-Márquez-Farías & Márquez-Romance, 2023): 1) 70.56 % and 0.6112; 2) 38.33 % and -0.23; 3) 83.00 % and 0.5662; 4) 84.4 % and 0.872, and 5) 85.0 % and 0.895, respectively.

2. The change/no change detection classification accuracy indices from the difference or ratio images suggest the following categorization in order from most to least accurate: a) difference brightness index obtained from the Kauth and Thomas method, b)

difference principal component No. 1 based on the reflectance image, c) difference reflectance images in the near-infrared spectral band; spectral band 4 on Landsat 5TM and 7 ETM, spectral band 5 on Landsat 8 OLI, d) difference NDVI vegetation index, and e) ratio reflectance images.

3. Despite what was stated in item 2, the method selected as having the greatest accuracy corresponds to the difference of the Principal Component No. 1; since the difference of the brightness index method proposed by Kauth and Thomas overestimates the areas of change/no change (Figures 17 and 18); this may be due to the fact that the adjustment coefficients or covariances in the multivariate linear regression are higher than that of the Principal Component No. 1. This aspect may be due to the influence of local characteristics of the spectral region such as solar angles, atmospheric conditions, land uses and covers on which the adjustment of the equation proposed by Kauth Thomas for Landsat MSS and its modifications for adaptation to the Landsat 5TM (Crist & Kauth, 1986) and 7 ETM sensors (Huang *et al*., 2002) was based. This aspect is supported because the variable used in multivariate linear regression corresponds to the digital number obtained from the n-dimensional space of the Landsat satellite spectral bands. As is known, this is the primary variable derived from Landsat satellite images; it lacks radiometric, topographic, or atmospheric corrections.

4. In the case of component No. 1 derived from the reflectance image, the aforementioned corrections were applied to a local scene predominantly covered by vegetation. Therefore, the reflectances contained in the spectral bands of the infrared spectral region are significantly higher than those of the other spectral bands. This results in the coefficients of these spectral bands being the highest in the

multivariate linear regression of Principal Component No. 1 of each image used in the bitemporal difference.

5. The difference in Principal Component 1 provides greater insight into the detection of changes/no changes in land uses and land covers than the difference in reflectance images in the near-infrared spectral band. This is explained by the fact that the regression coefficients between the reflectance contained in the spectral bands in the Landsat image and the Principal Component 1 were as follows: spectral bands 1, 2, and 3: $r > 0.96$; spectral bands 4 and 5: $r > 0.76$; and spectral band 7: $r > 0.86$; including most of the variance in these spectral bands; while the difference in spectral band 4 of the bitemporal reflectance image is limited to the variance of the reflectance in this spectral band only. The satisfactory result of the accuracy indices in the detection of changes for the difference method of reflectance images in the near-infrared spectral band is due to the fact that the scene has predominantly plant-based coverage and uses.

6. Vegetation index ratio and difference methods result in low accuracy rates in detecting changes/no changes in land cover and land uses; leaning towards detecting those areas with the same geographic position in bitemporal images simultaneously; where shadows and clouds occur; clear water bodies and water bodies with sediments and phytoplankton; irrigated agricultural soils and dry agricultural soils. This is explained by the fact that the reflectance from darkened or high humidity surfaces, which have a reflectance < 1 %, such as shadows, clear water bodies and irrigated soils, is extremely low, tending towards zero, compared to the reflectance from areas with: clouds, water bodies with sediments and phytoplankton, and dry agricultural soils (Markham & Barker, 1985; Bukata, Jerome, Borstad, Brown, & Gower, 2004; Karaska

et al., 2004; Jensen, 2009). Change/no change detection methods based on the ratio of reflectance images and difference of vegetation index images are sensitive to high reflectance differences (De-Márquez-Farías & Márquez-Romance, 2023).

Conclusions

Eight change detection methods have been evaluated; these have been classified as pixel-based methods. The methods included: post-classification (supervised classification applying maximum likelihood algorithm) and pre-classification (difference of reflectance images, regression of reflectance images, ratio of reflectance images, difference of normalized difference vegetation index images, analysis of change vector in reflectance images, transformation methods (principal components, Kauth and Thomas) . The post-classification methods have contributed, together with the pre-classification methods, to a better approximation of the proportion of the bitemporal areal difference associated with each land use/cover that occurred in the study area.

Categorizing the pre-classification methods in order from most to least accurate for estimating the bitemporal change/no change ratio of land covers and uses in the Pao River Basin from the error matrix and adjusting the methods to the local scene features in the Landsat satellite image resulted in: 1) principal component analysis, 2) image difference, 3) Kauth-Thomas transform, 4) change vector, 5) reflectance image ratio, 6) vegetation index image difference, and 7) image regression.

Among the pre-classification methods, the pixel-based change detection method with the greatest estimation capacity was the principal components method, using principal component number 1, compared to the other methods (image reflectance difference, image ratio, image regression, and normalized difference vegetation index difference). The image ratio, image regression, and normalized difference vegetation index difference methods include the greatest variance in reflectance values in the visible and infrared spectral regions for land use/cover: agricultural, grassland, and urban, as well as water, vegetation, and degraded land cover. These methods can be complemented by the change vector method to achieve better detection of changes associated with the transformation of land cover from water to vegetation, and vice versa. In addition, the change vector method has been useful as a complementary tool to estimate the proportion and direction angle of cover classes such as vegetation, water and soil.

The post-classification method allowed research intervention through a supervised classification of land uses and land covers in the Pao River basin, yielding satisfactory results with respect to the overall accuracy indices and Kappa index derived from the error matrix comparing the classified map with the reference image. This was applied to eleven images from the Landsat 5TM, 7ETM, and 8OLI satellites. After classification, an overlay tool led to the bitemporal land use and land cover change ratio for the period 1986 to 2016, represented through a change matrix. For the purposes of estimating change/no change in land uses and land covers, the post-classification method would be the predominant option over pre-classification methods.

References

Anderson, J. R., Hardy, E., Roach, J., & Witmer, R. (1976). *A landa-use and land-cover classification system for use with remote sensor data.* Washington, DC, USA: United States Government Printing Office. https://doi.org/10.3133/pp964

Araya, Y. H., & Hergarten, C. (2008). A comparison of pixel and object-based land cover classification: A case study of the Asmara region, Eritrea. *WIT Transactions on the Built Environment*, 100, 233-243. https://doi.org/10.2495/GEO080231

Bukata, R. P., Jerome, J. H., Kondratyev, K. Y., Pozdnyakov, D. V., & Kotykhov, A. A. (1997). Modelling the radiometric color of inland waters: Implications to a) remote sensing and b) limnological color scales. *Journal of Great Lakes Research*, 23(3), 254-269. https://doi.org/10.1016/S0380-1330(97)70910-9

Bukata, R. P., Jerome, J. H., Borstad, G. A., Brown, L. N., & Gower, J. F. (2004). Mitigating the impact of trans-spectral processes on multivariate retrieval of water quality parameters from case 2 waters. Canadian Journal of Remote Sensing, 30(1), 6-18. https://doi.org/10.5589/m03-046

Byrne, G. F., Crapper, P. F., & Mayo, K. K. (1980). Monitoring land-cover change by principal component analysis of multitemporal Landsat data. *Remote sensing of Environment*, 10(3), 175-184. https://doi.org/10.1016/0034-4257(80)90021-8

Chan, J. C. W., Chan, K. P., & Yeh, A. G. O. (2001). Detecting the nature of change in an urban environment: A comparison of machine learning algorithms. *Photogrammetric Engineering and Remote Sensing*, 67(2), 213-226. http://hdl.handle.net/10722/118210

Chander, G., Markham, B. L., & Helder, D. L. (2009). Summary of current radiometric calibration coefficients for Landsat MSS, TM, ETM+, and EO-1 ALI sensors. *Remote Sensing of Environments*, 113(5), 893-903. https://doi.org/10.1016/j.rse.2009.01.007

Chen, X., Chen, J., Shi, Y., & Yamaguchi, Y. (2012). An automated approach for updating land cover maps based on integrated change detection and classification methods. *ISPRS Journal of Photogrammetry and Remote Sensing*, 71, 86-95. https://doi.org/10.1016/j.isprsjprs.2012.05.006

Cakir, H. I., Khorram, S., & Nelson, S. A. (2006). Correspondence analysis for detecting land cover change. *Remote Sensing of Environment*, 102(3-4), 306-317. https://doi.org/10.1016/j.rse.2006.02.023

Collins, J. B., & Woodcock, C. E. (1996). An assessment of several linear change detection techniques for mapping forest mortality using multitemporal Landsat TM data. *Remote Sensing of Environment,* 56(1), 66-77. https://doi.org/10.1016/0034-4257(95)00233-2

Crist, E. P., & Kauth, R. J. (1986). The tasseled cap de-mystified. *Photogrammetric Engineering & Remote Sensing*, 52(1), 81-86. https://ntrs.nasa.gov/citations/19860037907

DeGloria, S. D., Laba, M., Gregory, S. K., Braden, J., Ogurcak, D., Hill, E., Fegraus, E., Fiore, J., Stalter, A., Beecher, J., Elliot, R., & Weber, J. (2000). Conventional and fuzzy accuracy assessment of land cover maps at regional scale. In: Heuvelink, G. B. M., Lemmens, M. J. P. M. (eds.). *Proceedings of the 4th International Symposium on Spatial Accuracy Assessment in Natural Resources and Environmental Sciences* (pp. 153-160). Delft, The Netherlands: Delft University Press.

De-Márquez-Farías, B. E. & Márquez-Romance, A. M. (2023). *Flood risk management sustainable plan in the Pao River basin, Carabobo state, from a community perspective* (Doctoral thesis). University of Carabobo, Valencia, Venezuela. http://riuc.bc.uc.edu.ve/handle/123456789/9479

Foody, G. M., & Mathur, A. (2004). Toward intelligent training of supervised image classifications: Directing training data acquisition for SVM classification. *Remote Sensing of Environment*, 93(1-2), 107-117. https://doi.org/10.1016/j.rse.2004.06.017

Foody, G. M. (2002). Status of land cover classification accuracy assessment. *Remote Sensing of Environment* 80, 185-201. https://doi.org/10.1016/S0034-4257(01)00295-4

Giri, C., Zhu, Z., & Reed, B. (2005). A comparative analysis of the Global Land Cover 2000 and MODIS land cover data sets. *Remote Sensing of Environment*, 94(1), 123-132. https://doi.org/10.1016/j.rse.2004.09.005

Guevara, E., & Cartaya, H. (2004). *Hydrology: An Introduction to Applied Hydrological Science*. Valencia, Venezuela: University of Carabobo.

Guerschman, J. P., Paruelo, J. M., & Burke, I. C. (2003). Land use impacts on the normalized difference vegetation index in temperate Argentina. *Ecological Applications*, 13(3), 616-628. https://doi.org/10.1890/1051-0761(2003)013[0616:LUIOTN]2.0.CO;2

Han, L., & Rundquist, D. C. (1997). Comparison of NIR/RED ratio and first derivative of reflectance in estimating algal-chlorophyll concentration: A case study in a turbid reservoir. *Remote Sensing of Environment*, 62(3), 253-261. https://doi.org/10.1016/S0034-4257(97)00106-5

Huang, C., Wylie, B., Yang, L., Homer, C., & Zylstra, G. (2002). Derivation of a tasselled cap transformation based on Landsat 7 at-satellite reflectance. *International Journal of Remote Sensing*, 23(8), 1741-1748. https://doi.org/10.1080/01431160110106113

Hussain, M., Chen, D., Cheng, A., Wei, H., & Stanley, D. (2013). Change detection from remotely sensed images: From pixel-based to object-based approaches. *ISPRS Journal of Photogrammetry and Remote Sensing*, 80, 91-106. https://doi.org/10.1016/j.isprsjprs.2013.03.006

INE, Instituto Nacional de Estadísticas. (2014). *XIV Censo Nacional de Población y Vivienda*. https://ine.gob.ve/wp-content/uploads/2024/09/Censo-Nacional-2011.pdf

Ingebritsen, S. E., & Lyon, R. J. P. (1985). Principal components analysis of multitemporal image pairs. *International Journal of Remote Sensing*, 6(5), 687-696. https://doi.org/10.1080/01431168508948491

Jensen, J. R. (2009). *Remote sensing of the environment: An earth resource perspective* (2nd ed.). Noida, India: Pearson Education India.

Joseph, G. (2005). *Fundamentals of remote sensing*. Hyderabad, India: Universities Press.

Karaska, M. A., Huguenin, R. L., Beacham, J. L., Wang, M. H., Jensen, J. R., & Kaufmann, R. S. (2004). AVIRIS measurements of chlorophyll, suspended minerals, dissolved organic carbon, and turbidity in the Neuse River, North Carolina. *Photogrammetric Engineering & Remote Sensing*, 70(1), 125-133. https://doi.org/10.14358/PERS.70.1.125

Kauth, R. J., & Thomas, G. S. (1976). The tasselled cap. A graphic description of the spectral-temporal development of agricultural crops as seen by Landsat. In: *LARS symposia* (p. 159). West Lafayette Indiana, USA: The Institute of Electrical and Electronics Engineers, Inc.

Kontoes, C. C. (2008). Operational land cover change detection using change vector analysis. *International Journal of Remote Sensing*, 29(16), 4757-4779. https://doi.org/10.1080/01431160801961367

Landis, J. R., & Koch, G. G. (1977). An application of hierarchical kappa-type statistics in the assessment of majority agreement among multiple observers. *Biometrics*, 33(2), 363-74. https://doi.org/10.2307/2529786

Lillesand, T., Kiefer, R. W., & Chipman, J. (2014). *Remote sensing and image interpretation*. Hoboken, USA: John Wiley & Sons. https://doi.org/10.5555/1215632

Lu, D., Mausel, P., Brondízio, E., & Moran, E. (2004). Change detection techniques. *International Journal of Remote Sensing*, 25(12), 2365-2401. https://doi.org/10.1080/0143116031000139863

Lunetta, R. S., Lyon, J. G., Guindon, B., & Elvidge, C. D. (1998). North American landscape characterization dataset development and data fusion issues. *Photogrammetric Engineering and Remote Sensing*, 64, 821-828. https://ostrnrcan-dostrncan.canada.ca/handle/1845/256499

Malila, W. A. (1980). Change vector analysis: An approach for detecting forest changes with Landsat. In: *LARS symposia* (p. 385). West Lafayette, Indiana, USA: The Institute of Electrical and Electronics Engineers, Inc.-Purdue University.

Markham, B. L., & Barker, J. L. (1985). Spectral characterization of the LANDSAT Thematic Mapper sensors. *International Journal of Remote Sensing*, 6(5), 697-716. https://doi.org/10.1080/01431168508948492

Mas, J. F. (1999). Monitoring land-cover changes: A comparison of change detection techniques. *International Journal of Remote Sensing,* 20(1), 139-152. https://doi.org/10.1080/014311699213659

Nackaerts, K., Vaesen, K., Muys, B., & Coppin, P. (2005). Comparative performance of a modified change vector analysis in forest change detection. *International Journal of Remote Sensing*, 26(5), 839-852. https://doi.org/10.1080/0143116032000160462

Nelson, R. F. (1983). Detecting forest canopy change due to insect activity using Landsat MSS. *Photogrammetric Engineering and Remote Sensing*, 49(9), 1303-1314. https://ntrs.nasa.gov/citations/19830065547

Richter, R., & Schläpfer, D. (2019). *Atmospheric and topographic correction (ATCOR theoretical background document)*. DLR IB, 1, 0564-03. https://www.rese-apps.com/pdf/atcor_atbd.pdf

Otukei, J. R., & Blaschke, T. (2010). Land cover change assessment using decision trees, support vector machines and maximum likelihood classification algorithms. *International Journal of Applied Earth Observation and Geoinformation*, 12, S27-S31. https://doi.org/10.1016/j.jag.2009.11.002

Rouse Jr., J. W., Haas, R. H., Schell, J. A., & Deering, D. W. (1974). Paper a 20. In: *Third earth resources technology satellite-1 symposium: The proceedings of a symposium held by Goddard space flight center at Washington, DC* (Vol. 351, p. 309). https://ntrs.nasa.gov/api/citations/19740025760/downloads/19740025760.pdf

Sedano, F., Gong, P., & Ferrao, M. (2005). Land cover assessment with MODIS imagery in southern African Miombo ecosystems. *Remote Sensing of Environment*, 98(4), 429-441. https://doi.org/10.1016/j.rse.2005.08.009

Sinha, P., & Kumar, L. (2013). Independent two-step thresholding of binary images in inter-annual land cover change/no-change identification. *ISPRS Journal of Photogrammetry and Remote Sensing*, 81, 31-43. https://doi.org/10.1016/j.isprsjprs.2013.03.010

Singh, A. (1989). Review article digital change detection techniques using remotely-sensed data. *International Journal of Remote Sensing,* 10(6), 989-1003. https://doi.org/10.1080/01431168908903939

Sohl, T. L. (1999). Change analysis in the United Arab Emirates: An investigation of techniques: Photogrammetric Engineering and Remote Sensing. *USGS Publications Warehouse*, 65(4), 475-484. https://pubs.usgs.gov/publication/70186963

Townshend, J., Justice, C., Li, W., Gurney, C., & McManus, J. (1991). Global land cover classification by remote sensing: Present capabilities and future possibilities. *Remote Sensing of Environment*, 35(2-3), 243-255. https://doi.org/10.1016/0034-4257(91)90016-Y

Trodd, N. M. (1995). Uncertainty in land cover mapping for modelling land cover change. In: *Proceedings of RSS95 remote sensing in action*. Lincoln, UK: Remote Sensing Society.

Ung, C.-H., Lambert, M.-C., Guidon, L., & Fournier, R. A. (2000). Integrating Landsat-TM data with environmental data for classifying forest cover types and estimating their biomass. In: Heuvelink, G. B. M., Lemmens, M. J. P. M. (eds.). *Proceedings of the 4th International Symposium on Spatial Accuracy Assessment in Natural Resources and Environmental Sciences* (pp. 659-662). Delft, The Netherlands: Delft University Press.

Vogelmann, J. E., & Rock, B. N. (1988). Assessing forest damage in high-elevation coniferous forests in Vermont and New Hampshire using Thematic Mapper data. *Remote Sensing of Environment*, 24(2), 227-246. https://doi.org/10.1016/0034-4257(88)90027-2

Yuan, F., Sawaya, K. E., Loeffelholz, B. C., & Bauer, M. E. (2005). Land cover classification and change analysis of the Twin Cities (Minnesota) Metropolitan Area by multitemporal Landsat remote sensing. *Remote Sensing of Environment*, 98(2-3), 317-328. https://doi.org/10.1016/j.rse.2005.08.006